Materials and Methods

1 Bacteria culture methods

1.1 Preculture

We purchased the *Alcanivorax borkumensis* SK2 type strain from ATCC (700651TM). *A. borkumensis* SK2 is an aerobic, non-motile, Gram-negative bacterium that can metabolize pyruvate and/or n-alkanes ranging from six carbons (C6) to more than C30 as the sole carbon and energy source *(10)*. Cells were cultured by streaking from a freeze stock onto Difco Marine Agar Plates (BD Difco; Marine Agar 2216) supplemented with 10 g/L (90 μM) sodium pyruvate (Sigma-Aldrich; P2256; CAS#113-24-6). After incubating the solid culture for 2 days (30°C), $\sim$5 isolated bacterial colonies were selected and inoculated in a test tube containing 4 mL of Marine Broth (MB) (BD Difco; Marine Broth 2216) supplemented with 10 g/L of sodium pyruvate (pyr); this culture medium is hereafter referred to as MB+pyr and was used exclusively for the preculture. This liquid culture was incubated in a linear axial shaker (Taitec, Japan) at 190 rpm at 30°C, which were used uniformly in all shaking liquid cultures. These steps are summarized in fig. S1A-1.

1.2 Main culture

Cells from the preculture were harvested after 2 days of incubation to start the main culture. The optical density of liquid cultures was measured at a wavelength of 600 nm (OD_{600}) using a Nanodrop spectrophotometer (Thermo-Fisher scientific, Nanodrop 2000/2000c UV-Vis). We used a chemically defined artificial seawater medium containing no carbon or energy sources, called ONR7a (Medium #950, DSMZ, Germany) for cell culturing. It is rich in nutrients relative to natural sea water. The cells were washed twice in ONR7a and resuspended in 4 mL at an OD_{600}=0.01 in a 15 mL glass test tube. The medium was supplemented with 100 μL of hexadecane (C16) (Sigma-Aldrich, 296317, CAS #544-76-3); we refer to this medium hereafter as ONR7a+C16 and it was used exclusively as the main-culture medium. This volume of C16 has a concentration of $\sim$85 μM in 4 mL, which is close to the concentration of sodium pyruvate in MB+pyr. Typically, multiple tubes of the main culture were simultaneously incubated under continuous shaking for a time ranging from 1 to 5 days (see fig. S1A-2).

Prior to OD_{600} measurements of liquid cultures containing oil, we rested the culture tube statically for 5 min to allow the emulsion to rise after removal from the incubator. To avoid the floating droplets, a long pipette tip was used to aspirate 100 μL of the cell culture

from the bottom of the test tube and the contents were transferred to a cuvette for the OD_{600} measurement. The growth curves measured in ONR7a+C16 are an approximate measure of cell growth in the presence of oil since inherently it does not account for cells attached to the floating oil droplets. Growth curves for *A. borkumensis* cultured in ONR7a+C16 and ONR7a+pyr are shown in fig. S1B, respectively.

1.3 Fluorescent strain construction

Fluorescent reporter strains were constructed by transforming *A. borkumensis* SK2 with plasmids containing either Pgap-gfp or Pgap-mCherry, which constitutively express GFP or mCherry, respectively. The nucleotides used for the plasmid construction are indicated in table S3. Briefly, the promoter sequence of the gap gene, which is constitutively expressed in *A. borkumensis (46)*, was cloned into the BamHI/EcoRI site of pPROBE-GT *(47)*. To replace GFP with mCherry on the fluorescence plasmid, we used In-Fusion HD Cloning Kit (Takara Bio). The nucleotide encoding mCherry, whose codon is optimized to *Pseudomonas aeruginosa*, was chemically synthesized (Eurofins Genomics). When culturing the fluorescent strains, 125 μM gentamicin was included in the media to prevent the loss of the fluorescent plasmid.

2 Microfluidic methods

2.1 Microfluidic device fabrication

Two-layer microfluidic devices were fabricated using two-step soft-lithography techniques. Briefly, the first layer of KMPR photoresist (Microchem, MA, USA) was spin-coated onto a silicon wafer and then exposed to i-line UV radiation through a photomask; this formed the channel layer. A second layer of photoresist was then spin-coated on top of the first layer, a second photomask was aligned using alignment marks in layer 1, and then exposed a second time; this formed the traps. Development of the unpolymerized KMPR revealed a two-layer master mold. We then poured well-mixed polydimethylsiloxane (PDMS) containing a curing agent (Dow Corning, Sylgard 184) in a 10:1 ratio onto the KMPR mold, degassed, and baked overnight at 75°C. The next day, the hardened PDMS slab was carefully peeled from the mold, holes were punched for inlet and outlet channels, and debris was removed using pressurized N2 gas. PDMS slabs and a cover glass were permanently bonded by bringing them together after oxygen plasma treatment (CUTE-MPR, FemtoScience, Korea) for 30 s at 100 W. A schematic of the filled device is

shown in fig. S2A.

2.2 Microfluidic device channel coating

We coated our microfluidic devices with polyvinyl alcohol (PVA) (Sigma-Aldrich; 363170; CAS #9002-89-5) to create a barrier preventing absorption of C16 *(48)*. To form this coating, immediately after plasma bonding, devices were submerged in a 2 wt% PVA dissolved in deionized filtered water (milliQ) solution and degassed under vacuum for 2 h. The devices were then flushed with pressurized N2 gas to remove the liquid and baked for 15 min at 110°C. We repeated this procedure 4x and then used the devices directly or stored them submerged in a 0.2 wt% PVA solution. This coating fully suppressed any measurable absorption of C16 by PDMS for up to 3 weeks (see fig. S2B).

2.3 Cell-laden drop generation

To generate cell-laden oil emulsion drops for trapping we harvested cells from the main culture. We washed the cells twice (16,000g for 5 min at 25°C), discarded the residual (conditioned) oil, and resuspended in ONR7a containing 0.1 wt% Tween 20 (Sigma-Aldrich; P9416; CAS# 9005-64-5) at a final OD_{600} of 0.75-1.0. To obtain this OD_{600} from the main culture after 1 day, we combined the contents of a $\sim$4 test tubes. At 5 days, only 1 tube of the main culture was used since the OD_{600} is sufficiently high. We then pipetted 100 μL of fresh C16 onto the washed cell suspension and vortexed (100 s at 3000 rpm), generating cell-laden oil emulsion drops with diameters in the range of 10-150 μm. We loaded the emulsion drops into a 5 mL syringe (Terumo, 5 mL Lock type syringe) for infusion into the device about 5 min after generation. This step is summarized in fig. S1A-3.

2.4 Device operation and droplet trapping

To operate the device, we connected a 10 mL syringe (Terumo, 10 mL Lock type syringe) to the device via a three-way valve (Terumo, 3-way stopcock), a blunt needle (Clay-Adams Intramedic 23 Gauge Luer-Stub adapter) and tubing (BD Intramedic PE50 tubing), directly to the media inlet (see fig. S2A). We then connected a 5 mL syringe (Terumo, 5 mL Lock type syringe) to the drop inlet port via a second three-way valve, blunt needle, and tubing. Both syringes were filled with ONR7a medium and used to prime the device by completely filling it with ONR7a medium. Special attention is paid to the removal of all trapped bubbles, which was achieved by strongly flushing additional

medium through the device. All effluent was collected from a tube connected to the outlet. After priming, the valves were closed.

The 5 mL syringe containing the emulsion was connected to the drop inlet port via the three-way valve. We infused the emulsion into device using a syringe pump (kdScientific Legato 200-788200). After a sufficient number of drops were trapped, we closed the valve connected to the drop inlet port. This step is summarized in fig. S1-4. We then washed the Tween 20 from the device by flushing ONR7a through the media inlet for 2 h at a flow rate (Q_{flow}) of 50 μL/min. We then set Q_{flow} = 0.5 μL/min, which is sufficient to replace the volume of media in the device once per minute, and initiated image acquisition.

2.5 Phenotype identification and isolation of DB-forming cells

We identified the biofilm phenotype from a test tube culture of a given age based on the drop deformation dynamics that we observed in bright-field and confocal time-lapse images over the course of 1-2 days (see fig. S3B,C for biofilm dynamics and Sec. 4.1 for imaging methods). Under our experimental conditions, we correlated the appearance of different phenotypes to culture time in presence of C16 (see fig. S1-5 for summary).

For convenience, we made freeze stocks of the DB phenotype to be able to more quickly regrow them. We isolated them by freezing samples from different test tubes of the main culture on day-5, prior to microfluidic identification. Each freeze stock consisted of 0.5 mL of the main culture combined with 0.5 mL of a sterile aqueous-glycerol mixture (50 vol% glycerol in DI water), and was stored at -80°C. We then identified the phenotype for each culture tube in separate microfluidic experiments. We kept the frozen samples that yielded the DB phenotype and discarded the others.

We confirmed that inoculation of the DB freeze stock into ONR7a+C16 yielded the DB phenotype. Here, we scraped the freeze stock using a sterile loop (As-One, 10 μL disposable PP loop) and inoculated one test tube containing 4 mL of ONR7a+C16, which was incubated for $\sim$24 h until it neared its stationary state. We then sub-cultured a few tubes, with fresh ONR7a+C16, setting the initial OD_{600} to 0.05 in each tube. These tubes reached their own stationary state in $\sim$20 h, at which point we confirmed their phenotype as DB using microfluidics. After this confirmation, we used the DB freeze stock to prepare DB cultures for the interfacial measurements, using the same protocol.

2.6 Measurement of the cell division time

For the cells grown using pyruvate we used a high-aspect ratio microfluidic device to facilitate the imaging of individual cells *(49)*. We determined the division time (t_{div}) by recording the interval between division events from individual cells for different generations and across different lineages. We determined t_{div} of the different phenotypes by recording the interval between division events of cells attached to trapped oil droplets. The division times for cells cultured in pyruvate is 1.74 $\pm$ 0.26 h, SB cells is 1.76 $\pm$ 0.21 h, and DB cells is 1.64 $\pm$ 0.23 h (see fig. S1D).

2.7 Fluorescent labeling of oil

To label the oil drops, we mixed the hydrophobic dye FM 4-64 (Thermofisher, CAS#: 162112-35-8) into the media at a final concentration of 2.5 μM and incubated at the start of the experiment. This dye also labels the cell membrane.

3 Interfacial properties

3.1 Separation of conditioned components

A. borkumensis is known to secrete biosurfactants *(50,10)* and other amphiphilic molecules *(32)* during cultivation with oil that may accumulate in the conditioned culture media or in the conditioned oil. To estimate how the different components of the liquid culture affect the interfacial tension (γ) of the aqueous/oil interface, we separated SB and DB liquid cultures into different components to measure each independently; these were: 1) live cells; 2) conditioned culture media; and 3) conditioned oil, respectively. For the SB phenotype, we harvested cells from the main culture after 24 h of incubation (see Sec. 1). For the DB phenotype, we regrew DB cells from a freeze stock following the protocol described in Sec. 2.5. Both phenotypes were harvested after about 20-24 h of incubation with fresh ONR7a+C16.

We harvested the components by centrifuging the liquid cultures (10 000 g for 30 min at 10°C), which simultaneously pelleted the cells and froze the C16 at the top of the media. We then gently transferred the frozen C16 and the supernatant to new tubes. We resuspended the cells in 1 mL and transferred the liquid to a new tube. Since the volume of conditioned oil in a single tube is less than 100 μL, we harvested from $\sim$20 tubes.

The cells were washed three times in fresh ONR7a ($10,000g$ for 30 min at 25°C), and we set the final $OD_{600}\approx$0.5 in 10 mL. We filter sterilized the conditioned supernatant by

passing it through a 0.22 μm pore filter (Merck Millipore). Finally, to remove cells and large cellular debris that may have been attached to the conditioned oil, we centrifuged it (20 000 g for 30 min at 25°C) three times, transferring the upper portion of the oil (leaving behind $\sim$100 μL) to a new centrifuge tube to minimize any carry-over of cells after each cycle. We note that small membrane fragments or hydrophobic molecules derived from lysed cells likely remain with the oil phase. The separation process is summarized in Fig. S6A.

3.2 Pendant drop tensiometry

We measured the interfacial tension (γ) of the aqueous/oil interface using a pendant drop tensiometer (Kyowa DM-305, Saitama, Japan). We tested γ between: 1) the harvested cells suspended in fresh ONR7a medium with fresh C16; 2) the cell-free conditioned ONR7a medium with fresh C16; and 3) conditioned C16 with fresh ONR7a medium. In each experiment, we filled a glass cuvette (3x3x2 cm^3) with the aqueous phase and vertically suspended a 5 μL oil pendant drop using a U-shaped needle attached to a 2.5 mL syringe and recorded images at regular intervals. The instrument software calculated γ as function of time and the plateau values are shown in fig. S6B-D.

3.3 Three-phase contact angle measurement

We measured the 3-phase contact angle (θ) between water, cells, and oil by measuring the angle between a water droplet that was deposited on a bacterial lawn that was submerged in C16 *(35)*. To form the lawn, we harvested cells from $\sim$10 tubes of the main culture of the desired phenotype (see Sec. 2.5); this number of tubes was used to ensured that we had enough cells. In each tube, we separated bulk oil from the liquid cultures by centrifuging (10 000 g for 30 min at 25°C) and resuspended the cells in milli-Q deionized water. We then washed the cells in milli-Q water ($16,000g$ for 10 min at 25°C) three times, resuspending in 10 mL and setting the final OD_{600} $\approx$1. Milli-Q water was used instead of a solution with dissolved salts to prevent salt crystals from forming in the bacterial lawn, which could affect the contact angle measurements. We removed any bacterial aggregates in this suspension that might create irregularities in the bacterial lawn by filtering with a 5 μm pore Durapore membrane filter (Merck Millipore Ltd.).

We generated the bacterial lawn by gently passing the cell suspension through a hydrophilic PVDF 0.45 μm pore Durapore membrane filter (Merck Millipore Ltd.) until it became clogged. For control experiments, we passed 10 mL of milli-Q water through the

membrane, drying it under the same conditions. We then carefully attached the filter to a glass slide (2.5x2.5 cm^2) using double sided tape, and dried it horizontally for 24 h at 30°C.

After drying, the filter was carefully submerged in an quartz cuvette (5x5x5 cm^3) containing 15 mL of C16. Any attached bubbles were dislodged with gentle pipetting. We then deposited a 12 μL drop of milli-Q water on the submerged bacterial lawn, and recorded θ using a contact angle measurement system (Kyowa DM-305, Saitama, Japan). We observed that after an initial spreading of the drop, θ plateaued over the course of a few minutes as the drop reached equilibrium. Images of water droplets on the different bacterial lawns are shown in fig. S7C-E.

3.4 Formation and trapping of cell-laden drops using conditioned oil

To test the effect of a reduced interfacial tension (γ) on biofilm phenotype, we generated cell-laden oil drops using SB-forming and DB-forming cultures using exclusively DB-conditioned oil, instead of fresh C16. Using the methods described earlier, we formed cell-laden oil drops on DB-conditioned oil, trapped them, and imaged for $\sim$24 h (see fig. S6E).

3.5 Interface competition test between SB and DB cells

Following the method described in earlier (see Sec. 2.5), we generated SB and DB cells that constitutively express mCherry and GFP, respectively. To prevent the loss of the plasmid during replication, 125 μM gentamycin was added to the culture media. We synchronized the culture times so that both SB and DB cells are formed on the same day. Then, we washed the respective cultures once and prepare a mixed suspension with a 3:1 ratio of SB to DB cells at an OD_{600} $\approx$1 in 5 mL. Next, we generated cell-laden oil droplets with the mixture and loaded the microfluidic device as described earlier. We acquired two-channel confocal images from $\sim$12 h, when the bacteria had nearly formed a monolayer. To prevent blurring we selected droplets with diameters that were approximately equal to the total height of the traps; these drops were free from movement. From the confocal images, we calculated the biovolume of the different phenotypes using Imaris 9.8 (Oxford instruments).

3.6 Mock Corexit formulation and characterization

We prepared a surfactant mixture similar to Corexit 9500 (Nalco Holding Company) because we were unable to obtain a commercial sample. We mixed surfactants bis-(2-ethylhexyl) sulfosuccinate (also known as DOSS) (Sigma-Aldrich; 323586; CAS#577-11-7) (18 wt%), Span 85 (Sigma-Aldrich; S7135; CAS#26266-58-0) (4.4 wt%), Tween 80 (Sigma-Aldrich; P1754; CAS#9006-65-6) (18 wt%), and Tween 85 (Sigma-Aldrich; P4634; CAS#9005-70-3) (4.6 wt%) following previously published estimates derived from analytical liquid chromatography *(51)*. We excluded an enantiomeric mixture of α- and β-ethyl hexylsulfosuccinate (α-/β-EHSS, 0.28 wt%) from our formulation since it is unclear whether or not it is an impurity.

We determined the critical micelle concentration (CMC) of our mock Corexit formulation by measuring the surface tension of the air/liquid interface (γ_{AW}) of ONR7a media containing different concentrations of it using a surface tensiometer (Kyowa DY-300, Saitama Japan). We estimated it to be 0.001 wt% (fig. S8C). We measured the interfacial tension (γ) between ONR7a medium containing different concentrations of the mock formulation with C16 using pendant drop tensiometry (fig. S8D).

3.7 Exposing dendritic biofilms to our mock Corexit formulation

We exposed DBs growing on trapped droplets for 6-8 h to different concentrations of our formulation ranging from 25× to 100×CMC. For the experiments shown in fig. S8A, we used a concentration of 0.05 wt% (50×CMC). For reference, this concentration is $\sim$20x greater than the estimated concentration of Corexit in the top 20 cm of the ocean post-application during the Deepwater Horizon accident *(37)*. To precisely detect the entry time into the droplet chamber, we added 3 μM FITC (Sigma-Aldrich, 34321-M, CAS No. 3326-32-7) to the culture media and acquired bright-field and fluorescent images at the outlet of the device (see fig. S2A for port location). This method allowed us to use media fluorescence as a proxy for our mock Corexit concentration (fig. S8E). Approximately 100 min are required for the steady state concentration in the device to be reached after infusion.

4 Imaging and analysis

4.1 Brightfield and confocal imaging

We tracked biofilm development on C16 droplets by acquiring either bright-field (Zeiss Axio observer) or confocal (Zeiss LSM 780 or Olympus SPINSR10) time-lapse sequences over the course of 1-4 days. When we used the Axio observer, we used a stage heater (Tokai-Hit, Shizuoka, Japan) to maintain a temperature of 30°C. The confocal microscopes are both equipped with incubators that maintain 30°C. Both the LSM 780 and SPINSR10 have enhanced resolution modes, called Airy scan or confocal 'super' resolution, respectively. We typically used 63x or 100x oil immersion lenses with numerical apertures (NA) of 1.40 or 1.46. Confocal images are rendered using Imaris 9.8 (Oxford instruments). Unless explicitly stated, microscopy images in the main text are maximum intensity projections of the acquired stacks.

During confocal imaging, we used strains that constitutively express fluorescent proteins EGFP and mCherry or we labelled the bacteria with fluorescent membrane dyes such as FM 4-64 or FM 1-43 (Thermo-Fisher Scientific; F34653) by adding it to culture medium flowing in the device. To visualize WT cells at the oil-water interface, we added fluorescein isothiocyanate (FITC) (Thermo-Fisher Scientific; F1907; CAS#3326-32-7) at a concentration of 0.5-1 μM to the medium. FITC readily labels the cells but has low affinity for C16.

4.2 Drop radius, surface area, and volume measurements

For spherical biofilms (SBs), since the shape of the oil droplets remain approximately spherical as they are consumed until $\sim$72 h, we measured the droplet radius (R) at its equator and use it to calculate surface area $S(t) = 4\pi R(t)^2$ and droplet volume $V(t) = \frac{4}{3}\pi R(t)^3$. For dendritic biofilms (DBs), since the oil droplet deforms soon after monolayer formation, the drop radius is ill defined. To estimate surface area at each time point, we drew closed contours along the fluorescent interface using Imaris in each plane of confocal images and combined them using the 'surface' function to create a surface. We measured surface area from this object.

We calculated S and V as follow: $S = \sum_0^m P_i \Delta z$ and $V = \sum_0^m A_i \Delta z$, where m is the number of z-plane slices that span the droplet, P_i is the perimeter of i-th contour line, Δz is the height resolution in the z direction, and A_i is the i-th contour line enclosing an area. We typically used $\Delta z \sim$ 1-2 μm.

4.3 Generating a surface from bright-field image sequences

We estimated the shape from a set of bright-field images using algorithms written in MATLAB *(52,53)*. These algorithms determine the focus for each pixel in a local window in an image sequence with different focus, which is then used to reconstruct the shape. For the focus measurement, we used a gradient-based operator that calculates focus from the first derivatives of the image with the assumption that focused images present sharper edges than those of out-of-focus images. The shape reconstruction technique is based on the Gaussian model of defocus. In this technique, pixels with the highest focus values are identified in the image, and then a depth map is constructed by interpolating a Gaussian function around this pixel. A local focus window size of 1.5-2 μm generated realistic drop shapes.

4.4 Nematic order and defect detection in focus-stacked images

We detected topological defects of charge $\pm 1/2$ defects using publicly available code *(14)*. In addition to these, we also identified ± 1 defects based on the structure of the defect. We used the following steps to detect defects: 1) generate focus-stacked image sequences; 2) calculate the orientation field from these sequences; and 3) detect defects.

Focus stacking fuses the in-focus regions from multiple bright-field images taken at different focal positions of the same region of interest (ROI) into a single image; thus generating an image with larger depth-of-field. We used these to analyze the curved droplet surface. We generated focus-stacked images using a publicly available MATLAB algorithm *(54)*. Briefly, the algorithm works in three stages: 1) focus measurement; 2) selectivity measure; and 3) image fusion. The regions of focus are measured using gray level local variance, selectivity is estimated from pixel focus to noise ratio, and fusion is performed according to focus measure and features of image pixels categorized by selectivity strength. We obtained focus-stacked image sequences with the following settings: local focus window size = 0.8 – 1.4 μm; selectivity threshold = 0.4 – 0.7 μm; and selectivity constant: 0.1 – 0.3.

To calculate the orientation field for each pixel, we used the OrientationJ plugin in ImageJ (v1.53f51) on focus-stacked images. This program generates the orientation field for each pixel using the tensor method, where we set the local structure window size that defines spatial scale for the orientation field calculation. The accuracy of defect detection mainly depends on the local window size: choosing smaller windows results in false positives, while larger windows smooth the orientation field, suppressing defects *(55)*. We

obtained the best results for a window size of 0.5 μm, which is half the diameter of a bacterium. The structure window size defines the spatial scale over which the orientation field is calculated, and the output is a 32-bit image with an orientation for each pixel with values ranging from -90° to $+90^{\circ}$. Next, from the orientation field images using MATLAB written code publicly available on GitHub *(14)*, we detected topological defects, their position and direction, and overlaid on the original focus stacked images.

From the orientation field, we calculated the director field by dividing the orientation image into $j \times k$ square grids and obtained vector s by summing the orientations of all pixels in each grid. We used a grid with a 2 μm diagonal, which is the length of an average cell. To estimate the local nematic ordering, we calculated the nematic order parameter using the equation $Q = \sqrt{\langle \cos(2\phi) \rangle^2 + \langle \sin(2\phi) \rangle^2}$, where ϕ is the orientation angle and the brackets denote the average for a local window of size 35 μm^2 *(56,14)*.

4.5 Cell alignment on oil tubes

To calculate the degree of alignment of cells along oil tubes, we calculated the average of the dot products between each cell's orientation vector with the tangent vector of the tube axis in bins of 1.45 μm. To do this, we first generated a focus-stacked image from confocal slices of an oil tube and then calculated the director for each cell. We then generated the curvilinear axis of the tube that runs along the center, and calculate the unit tangent vector, $\boldsymbol{n}_{\text{tube}}$, in 1.45 μm width bins. We then calculated $\langle \boldsymbol{n}_{\text{cell},i} \cdot \boldsymbol{n}_{\text{tube}} \rangle$, where $\boldsymbol{n}_{\text{cell},i}$ is the unit vector of the i-th cell in bins of 1.45 μm along the tube axis and the angled brackets represent the average over all cells within the bin.

4.6 Oil tube length measurement

We measured the oil tube length by defining a central axis running from its base to the tip. We assumed that functional form for tube elongation is exponential since cell division appears to drive tube elongation and because cells are highly aligned with the central axis of the oil tube (Fig. 2D,E). We fitted an equation of the form $l_{tube} = L_0 \exp(t/\tau_{tube})$ to the mean value of all tube lengths, where l_{tube} is the length of the tube, L_0 is the initial tube length, t is time, and τ_{tube} is the time constant, shown as the dashed line in Fig. 2F. We fit both L_0 and τ_{tube}. We find that the time required for the tubes to double in length is $\sim$ 3.36 h ($\sim$ 200 min), which is about twice of the cell division time, t_{div}, of 1.65 h.

4.7 Pseudo color image generation

We generated the pseudo color images using ImageJ plugin 'Z-stack Depth Colorcode 0.0.2'.

5 Statistics and reproducibility of experiments

The statistical significance was determined using Welch's unequal variances t-test with the Holm-Bonferroni post hoc correction applied when needed. Statistical data are presented as average $\pm$ standard deviation (SD). The sample size (n), number of independent replicates, and p-values are specified in the figure legends. When image data from a single sample are shown, they are representative of at least three additional samples from independent experiments. We used MATLABv2020 and Origin 2019 for data analysis.

Supplementary Text

1 Principle of surface-tension droplet trapping

Our device utilizes the oil-water interfacial tension to trap the drops in vertically-oriented cylindrical pockets (see Fig. 1A and fig. S2A) *(57)*. As the emulsion is flowed through the device, drops whose diameters are larger than the height of the main channel are flattened into disks, while smaller droplets remain spherical. When the flattened droplets encounter a vertical pocket, they can reduce their surface-to-volume ratio by becoming more spherical; this traps the droplets in place. Some fraction of the drops become trapped while the rest are washed away. The continuous flow of fresh medium and access to oxygen enables the cells to proliferate on the trapped oil drops.

2 Bacterial adaptation and biofilm formation

The spherical biofilm (SB) phenotype appears on trapped drops using cells that were collected from the main culture after 1 d (fig. S3B). The dendritic biofilm (DB) phenotype appears on drops when using cells collected after 5 d, at a lower frequency (fig. S3C). At an intermediate period of time of 3-4 d, we find an intermediate state that possesses characteristics of both the SB and DB phenotypes, such as thin biofilms that cause only small-scale deformations, relatively short oil tubes, and an oil degradation rate similar to SBs. At times, some biofilm covered droplets from these intermediate cultures show an oscillatory behavior, alternating between the SB- and DB-like phenotypes. For this reason, we designate this mixed intermediate state as the oscillatory biofilm (OB) phenotype (fig. S9).

We find that OBs and DBs develop in $\sim$20% of the liquid cultures that we inoculated. To ensure sufficient sampling we typically cultured $\sim$10 test tubes to select the OB or DBs, from which we independently tested 4 tubes using microfluidics. In addition to differences in oil degradation dynamics, the test tube cultures also show qualitative differences that are evident by inspection at day-5 (fig. S1C). We find that tubes that yielded the SB phenotype tended to have lower OD_{600} and a sedimented biofilm attached to the tube wall near the bottom. The OB and DB phenotypes typically had higher OD_{600}, smaller emulsion drops than the SB tubes, and lacked significant accumulation of biofilm at the tube bottom. The size of the emulsion drops in DBs tubes were significantly smaller than OB emulsions, as shown in fig. S1C.

3 Analytical model of oil consumption

We assume that the consumption of oil is mediated by bacteria attached directly to the oil/water interface, such that the time rate-of-change of the oil volume reads:

$$\frac{\mathrm{d}V(t)}{\mathrm{d}t} = -\alpha N(t), \tag{1}$$

where $V(t)$ is the volume of oil, $N(t)$ is the number of interfacial bacteria, and α is the oil consumption rate per bacteria. We will define α_{SB} and α_{DB}, with subscripts to differentiate the consumption rate in both phenotypes. The maximum number of cells that can lie flat on the interface at a given time is:

$$N(t) = \frac{S(t)}{s_c} c_{\mathrm{pf}} = S(t)\rho_H, \tag{2}$$

where S is the total surface area at the oil/water interface, s_c is cross-sectional area of a cell, and c_{pf} is the cell packing fraction, which we estimate to be 0.65*(58)*; $\rho_H = c_{\mathrm{pf}}/s_c$ is the density of bacteria. We estimate that s_c = 1.8 μm^2 for cells 2 μm in length and 1 μm in diameter (fig. S11B). Substituting Eq. (2) into Eq. (1), we have:

$$\frac{\mathrm{d}V(t)}{\mathrm{d}t} = -\frac{\alpha c_{\mathrm{pf}}}{s_c} S(t). \tag{3}$$

3.1 Oil consumption by spherical biofilms

In the SB phenotype, the oil volume remains approximately spherical as SBs consume the oil. We substitute $4\pi R(t)^3/3$ for $V(t)$ and $4\pi R(t)^2$ for $S(t)$ in Eq. (3), which allows us to relate the time rate-of-change of $R(t)$ to the oil consumption rate of a single cell from the SB phenotype, α_{SB}. Simplifying, we find that:

$$\frac{\mathrm{d}R(t)}{\mathrm{d}t} = -\frac{\alpha_{\mathrm{SB}} c_{\mathrm{pf}}}{s_c} = -\sigma_{\mathrm{SB}}. \tag{4}$$

Integrating Eq. (4), we obtain $R(t) = R_0 - \sigma_{\mathrm{SB}} t$, which we can then normalize by the initial value of the radius (R_0), leading to:

$$R^*(t) = \frac{R(t)}{R_0} = 1 - \sigma^*_{\mathrm{SB}} t, \tag{5}$$

where $\sigma^*_{\mathrm{SB}} = \sigma_{\mathrm{SB}}/R_0$. This equation agrees with our measurements of drop radii, where we find that the time rate-of-change of $R^*(t)$ is a constant, as shown in Fig. 1D(inset). The best fit slope to the $R^*(t)$ data in Fig. 1D(inset) yields $\sigma^*_{\mathrm{SB}} = 0.008$ h^{-1}. Similar values

are obtained for σ^*_{SB} when fitting S^* or V^* in Fig. 1D,E through the surface and volume relations:

$$S^*(t) = (1 - \sigma^*_{\mathrm{SB}} t)^2, \quad \text{and} \quad V^*(t) = (1 - \sigma^*_{\mathrm{SB}} t)^3. \tag{6}$$

From our data of droplet size decrease, we find that $\sigma_{\mathrm{SB}} = 0.26\,\mu\mathrm{m/h}$, for $R_0 = 32 \pm 2\,\mu\mathrm{m}$. Using these values with Eq. (4), we estimate the average single-cell consumption rate $\alpha_{\mathrm{SB}} = 0.7\,\mathrm{fL/h}$. For reference, the volume of a single cell is $\sim$1 fL.

In this model, we assumed that all cells lie flat along the interface, that they all have the same dimensions, and that interfacial cell density ρ is constant.

3.2 Oil consumption by dendritic biofilms

Since dendritic biofilms (DBs) strongly deform the oil volume, we are unable to approximate the decreasing oil volume as a sphere and thus unable to relate V and S to R. Although we assume Eqn. (1)-(3) still apply, in this case, we assume that cell division drives the deformations, and therefore that the increase in surface area has an exponential functional form.

From the measured division time, t_{div}, we calculate the exponential time constant as $\tau = t_{\mathrm{div}}/\ln 2 \approx 2.4$ h (fig. S1D). To determine the change in N at the oil-water interface, we assume that it scales exponentially with time as:

$$N(t) = N_0 \exp\left(\frac{ft}{\tau}\right), \tag{7}$$

where we include a fitting factor f, which represents the fraction of cells at the interface that participate in increasing the interface area. In Sec. 6.3.3, Eq. (33), we relate f to the existence of a flux of cells ejected from the interface, into a thick biofilm, which we observe experimentally in movies S1-3 and S5. Combining Eq. (2) and (7), we predict that the interfacial area grows exponentially:

$$S(t) = \frac{s_c}{c_{\mathrm{pf}}} N_0 \exp\left(\frac{ft}{\tau}\right), \tag{8}$$

which we normalize with the initial value S_0, leading to:

$$S^*(t) = \exp\left(\frac{ft}{\tau}\right). \tag{9}$$

We fit the S^* data in Fig. 1D using Eq. (9) with f as the only fit parameter, which yields a value of $f = 0.11 \pm 0.01$. According to Eq. (7), this value indicates that $\sim$11% of all cells participate in increasing the surface area (see fig. S11A). Such a value is consistent

with the homeostatic growth model with the oil surface having a constant elongation rate discussed later in Sec. 6.3.3. Substituting Eq. (8) into Eq. (3) yields:

$$\frac{\mathrm{d}V}{\mathrm{d}t} = -\alpha_{\mathrm{DB}} N_0 \exp\left(\frac{ft}{\tau}\right) = -\sigma_{\mathrm{DB}} S_0 \exp\left(\frac{ft}{\tau}\right), \tag{10}$$

where $\sigma_{\mathrm{DB}} = \alpha_{\mathrm{DB}} \cdot c_{\mathrm{pf}}/s_c$. Integrating Eq. (10) and utilizing the fact that the droplet is still spherical at $t_0 = 0$, we find that

$$V^*(t) = \frac{V}{V_0} = 1 + 3\sigma^*_{\mathrm{DB}} \frac{\tau}{f}\left[1 - \exp\left(\frac{ft}{\tau}\right)\right], \tag{11}$$

where $\sigma^*_{\mathrm{DB}} = \sigma_{\mathrm{DB}}/R_0$. Fitting the experimental data with the expression provided in Eq. (11), we find that $\sigma^*_{\mathrm{DB}} = 0.009\ \mathrm{h}^{-1}$. For an oil droplet with $R_0 = 32\ \mu\mathrm{m}$, we find that $\sigma_{\mathrm{DB}} = 0.3\ \mu\mathrm{m\ h}^{-1}$ and the consumption rate per cell $\alpha_{\mathrm{DB}} = 0.8\ \mathrm{fL\ h}^{-1}$. Thus, our findings indicate that in the DB phase, while the single-cell consumption rate is approximately 12% higher than in the SB phase, the notable disparity in the rate of volume change between the two phenotypes is primarily attributed to the exponential growth in interfacial area.

3.3 Surface-to-volume ratio

In the SB phase, the normalized surface-to-volume ratio is:

$$\frac{S^*}{V^*} = (1 - \sigma^*_{\mathrm{SB}} t)^{-1}, \tag{12}$$

whereas in the DB phase, it is:

$$\frac{S^*}{V^*} = \frac{\exp\left(\frac{ft}{\tau}\right)}{1 - 3\sigma^*_{\mathrm{DB}} \frac{\tau}{f}\left(\exp\left(\frac{ft}{\tau}\right) - 1\right)}. \tag{13}$$

These equations are used to plot the dashed lines in Fig. 1E(inset) using the derived values.

4 Topological Defects

The nematic orientational field can be characterised by a director field $\hat{n}$ with $|\hat{n}| = 1$ that represents the local coarse-grained orientation of assemblies of microscopic constituents, in our case bacteria. To reflect the head-tail symmetry characterising a nematic phase, the director field presents the symmetry $\hat{n} \to -\hat{n}$ (i.e. it is invariant to a rotation of $180°$). In two dimensions, the director field can be expressed as $\hat{n} = (\cos(\phi), \sin(\phi))$, where ϕ is the angle of the director field with an arbitrary axis on the xy plane. The

degree of nematic order is quantified by the nematic order parameter that is defined as $Q = \sqrt{\langle\cos(2\phi)\rangle^2 + \langle\sin(2\phi)\rangle^2}$, where the symbol $\langle\cdot\rangle$ denotes a local average over a local region of interest. For a perfectly aligned nematic phase $Q = 1$, and for a perfectly disordered phase $Q = 0$.

Nematic topological defects are regions where the nematic orientational field is undefined, which corresponds to regions where the nematic order parameter Q vanishes. In two dimensions, topological defects are characterized by the topological charge $q = \Delta\Theta/(2\pi)$, where $\Delta\Theta$ is the net angle through which the director field $\hat{n}$ rotates as one follows a closed path encircling the topological defect. The standard convention is that the topological charge is positive when the direction of rotation of the director field is the same as the path traversed, and otherwise it is negative. For two-dimensional nematic liquid crystals, topological defects can have a topological charge that is a multiple of a half-integer $q = \pm m/2$, where m is an integer number. Defects with topological charges of $\pm 1/2$ and ± 1 are shown in fig. S4A.

5 Adhesion energy at the interface

The adsorption energy (G) of a particle at the oil-water interface corresponds to the work required to detach the particle from the interface; this energy is given by:

$$G = \gamma s(1 - |\cos\theta|)^2, \tag{14}$$

where γ is oil/water interfacial tension, *s* is the interfacial area occupied by the particle, and θ is the 3-phase contact angle of the particle *(59)*. This equation assumes that the particle is in equilibrium, meaning that it is wetted uniformly around its perimeter. The trapping energy for 1 μm passive particles is on the order of $\sim 10^7\ k_B T$, where k_B is the Boltzmann constant, and T is temperature. Typical systems at (or near) room temperature can supply energies of about 1-10 $k_B T$, implying that the particle is essentially trapped at the interface.

Bacterial surfaces differ significantly from the surfaces of polystyrene or silica particles that are commonly used as Pickering stabilizers of oil-in-water emulsion droplets. These particles are passive and have homogeneous surfaces. In contrast, bacterial surfaces are decorated with adhesive proteins, called adhesins, which are, in general, not distributed evenly across the surface; this likely changes the local adhesion value. How Eq. (14) should be modified to account for the heterogeneous nanostructure of the bacterial surface is still an open question. In addition, bacteria *(21)* can attach to oil/water interfaces in non-equilibrium orientations, further complicating the actual adhesion energy.

Bacterial division at oil-water interfaces leads to a mechanical stress accumulation in the biofilm at the interface as soon as a confluent monolayer is reached. The extensional growth pressure of *Pseudomonas aeruginosa* is of the order of 1 MPa *(39)*, which corresponds to a μN force applied over the cross-section of the cell. If we assume the same for *A. borkumensis*, the work done by the cell is 10^{-12} J over a distance of 1 μm, which corresponds to $\sim 10^8\ k_B T$. Thus, for cells in equilibrium, cell elongation could provide the energy to detach the bacteria, causing them to stand vertically or detach from the interface entirely.

6 Membrane model for spontaneous tube formation

6.1 General free energy

Here, we model the biofilm at the oil/water interface as a liquid crystal membrane. The membrane is defined by a metric g, a curvature tensor C and a normal vector $\mathbf{e}_n$. The bacteria orientation is represented by the director field $\mathbf{n}$. We consider that the orientational order is well developed (i.e. $|\mathbf{n}| = 1$). We consider the following free-energy that preserves the nematic symmetry (i.e. $\mathbf{n} \to -\mathbf{n}$),

$$\mathcal{F} = \int da \left\{ \gamma + \frac{\kappa_{B,\parallel}}{2} \left(n^i n^j C_{ij} - C_{\parallel,0} \right)^2 + \frac{\kappa_{B,\perp}}{2} \left(n^i_\perp n^j_\perp C_{ij} - C_{\perp,0} \right)^2 + \frac{\kappa_F}{2} (\nabla_i n_j)(\nabla^i n^j) \right\}, \tag{15}$$

where

- da the element of area along the surface and the integral is over the surface of interest;
- γ is the surface tension;
- $\kappa_{B,\parallel}$ and $\kappa_{B,\perp}$ (resp. $C_{\parallel,0}$ and $C_{\perp,0}$) are the bending rigidities (resp. preferred curvature) of the biofilm in the parallel and perpendicular direction to the local nematic order $\mathbf{n}$ field; $\mathbf{n}_\perp = \mathbf{e}_n \times \mathbf{n} / |\mathbf{e}_n \times \mathbf{n}|$ defines the orthogonal direction to the nematic field along the membrane;
- κ_F is an elastic constant, penalizing distortions of the director field. The operator ∇_i is the covariant derivative *(42)*.

6.2 Simplified static model

6.2.1 Mechanical stability of a biofilm tube

Tube geometry: We focus on the mechanical stability of a tube of radius r. The bacteria main axis of elongation is oriented along the tube z direction, i.e. $\mathbf{n} = (0, 0, 1)$ in Cartesian coordinates. As we assume the director field to be fixed, we disregard energy variations due to distortions of the director fields; further, considering $C_{\parallel,0} \approx 0$, the second term in Eq. (15) vanishes. Therefore, in the cylindrical coordinates (r, θ, z), with θ the azimuth coordinate (fig. S14), Eq. (15) simplifies into

$$\mathcal{F} = \int 2\pi r dz \left[\frac{\kappa_B}{2} \left(\frac{1}{r^2} - \frac{2C_{\theta,0}}{r} \right) + \gamma \right] = f_z(r) \int dz, \tag{16}$$

where $C_{\perp,0} = C_{\theta,0}$ is the spontaneous curvature in the θ direction and where we use the notation $\kappa_B = \kappa_{B,\perp}$; the integral spans over the tube surface. In Eq. (16), we defined f_z, the free energy per unit length along the z axis. At equilibrium, the normal force balance on the tube reads

$$dr \frac{\partial f_z}{\partial r} = 2\pi r \Delta P dr, \tag{17}$$

where ΔP is the pressure difference between the inside and outside of the tube. Expressed in terms of Eq. (16), Eq. (17) reads

$$\gamma + \frac{\kappa_B}{2} \left(-\frac{1}{r^2} \right) = r\Delta P. \tag{18}$$

Here, we consider that the pressure within the tube is the same as the pressure within the rest of the oil droplet, which we approximate as a sphere of radius $R_d \gg r$. The pressure difference within the spherical part of the oil droplet is given by the Laplace law

$$\Delta P = 2\gamma / R_d, \tag{19}$$

which corresponds to Eq. (18) but in a sphere geometry. The right-hand side of Eq. (18) then scales as $r/R_d \ll 1$, which amounts to a small perturbation. Henceforth, we neglect the effect of pressure differences (i.e. $\Delta P = 0$) in the rest of our calculation. The expression of the radius r_{eq} that satisfies the normal force balance condition Eq. (18) then takes the particularly simple expression:

$$r_{\mathrm{eq}} = \sqrt{\frac{\kappa_B}{2\gamma}}. \tag{20}$$

While Eq. (20) is independent of the value of the spontaneous curvature $C_{\theta,0}$, the stability of a tube of radius $r = r_{\rm eq}$ depends on the spontaneous curvature $C_{\theta,0}$. Indeed, the force needed to pull the tube along the z direction

$$f_z = \frac{d\mathcal{F}}{dz}, \tag{21}$$

can be expressed in terms of the solution $r_{\rm eq}$ to Eq. (18) as

$$f_z = 2\pi r_{\rm eq}\left(2\gamma - \frac{\kappa_B C_{\theta,0}}{r_{\rm eq}}\right). \tag{22}$$

The tube shrinks whenever $f_z > 0$ and expands otherwise. The tube stability condition $f_z = 0$ is reached for the radius

$$r'_{\rm eq} = \frac{\kappa_B C_{\theta,0}}{2\gamma}, \tag{23}$$

which, in contrast to Eq. (20), depends on the value of the spontaneous curvature. Based on Eq. (20) and Eq. (23), the condition $r'_{\rm eq} = r_{\rm eq}$ yields the threshold spontaneous curvature for tube formation:

$$\gamma = \kappa_B C_{\theta,0}^2/2, \tag{24}$$

which, under the notation $C_{\theta,0} = 1/r_0$, corresponds to Eq. (1) in the main text.

6.2.2 Relation to the bacteria density

We expect the mechanical parameters (bending modulus, spontaneous curvature, and tension) that describe the biofilm to depend on the bacteria density. Here, we consider the expansion at second order in the density field

$$(\gamma - \kappa_B C_{\theta,0}^2/2)_{|\rho} \sim k_0 - k_1\rho + k_2\rho^2. \tag{25}$$

As the oil/water interface displays no obvious spontaneous curvature in the absence of bacteria ($\rho = 0$), we expect that $k_0 = \gamma_0 > 0$, where γ_0 is the surface tension in the absence of bacteria. We are then led to define the function

$$\kappa(\rho) = \gamma_0 - k_1\rho + k_2\rho^2. \tag{26}$$

such that the condition of Eq. (24) is met for $\kappa(\rho) = 0$ and that tube formation occurs for $\kappa(\rho) < 0$. We further justify the expansion in ρ in the next section, Sec. 6.3.3. The phenomenology corresponding to Eq. (26) is further discussed in Sec. (7.3).

6.3 Dynamical model

In this section, we make use of the theoretical framework developed in Ref. *(60)* to study the tube formation dynamics of a nematic liquid crystal membrane.

6.3.1 Conservation of the bacteria mass

Along the membrane surface, the balance in the density of bacteria ρ can be expressed as:

$$\frac{\partial \rho}{\partial t} + \nabla_i \left(\rho v^i\right) + v_n C_i^i \rho = k(\rho)\rho, \tag{27}$$

where

- ∇_i is the covariant derivative, $\mathbf{v} = v^i \mathbf{e}_i + v_n \mathbf{e}_n$ is the local velocity with $\mathbf{e}_i$ basis vectors in the membrane frame of reference and v_n the velocity along the outward-oriented normal vector $\mathbf{e}_n$ to the membrane surface;
- k is the rate of bacteria turnover, which is immediately related to the parameter f defined in Eq. (7). Here, we expand k in the vicinity of homeostatic conditions $k(\rho) = k_d(1 - \rho/\rho_H)$; for $\rho < \rho_H$, bacteria divide more than they die (or leave the interface), and $k(\rho)$ is a source term; for $\rho > \rho_H$, bacteria are ejected more than they divide, and $k(\rho)$ is a sink term.

We first focus on the case of a tube of radius r. As discussed Sec. (6.3.2), we will assume a fast mechanical relaxation along the normal direction (i.e. $v_n = \partial r/\partial t = 0$). In this case, Eq. (27) reads

$$\frac{\partial \rho}{\partial t} + v_z \partial_z \rho + \rho \left(\partial_z v^z\right) = \rho k_d \left(1 - \frac{\rho}{\rho_H}\right). \tag{28}$$

Furthermore, we will neglect spatial heterogeneities along the tube direction, e.g. we assume that $\partial_z \rho = 0$ (uniform bacterial concentration) and that the tube expansion rate $\partial_z v^z$ is constant, which implies that

$$\partial_z v^z = \frac{1}{L}\frac{dL}{dt}, \tag{29}$$

where L is the total tube length. Under these assumptions, Eq. (28) amounts to

$$\frac{d\rho}{dt} + \frac{\rho}{L}\frac{dL}{dt} = \rho k_d \left(1 - \frac{\rho}{\rho_H}\right). \tag{30}$$

We point out two specific features of Eq. (30):

1. Defining a total number of bacteria $N = \rho(2\pi r L)$, we find that

$$\frac{dN}{dt} = N k_d \left(1 - \frac{\rho}{\rho_H}\right), \tag{31}$$

such that the number of bacteria in the biofilm is constant only if $\rho_H = \rho$.

2. In the case of a constant tube growth rate and at steady state ($d\rho/dt = 0$), the bacterial density reads

$$\rho_{ss} = \rho_H \left(1 - \frac{1}{k_d L}\frac{dL}{dt}\right), \tag{32}$$

which describes a *dilution* effects: the faster the tube grows, the lower the steady-state density (ρ_{ss}) is with respect to the homeostatic density (ρ_H).

In the case of a constant tube elongation rate $(dL/dt)/L$, the density ρ_{ss} defined in Eq. (32) is a constant; in this case, Eq. (31) yields an expression consistent with Eq. (7), with

$$f = k_d(1 - \rho_{ss}/\rho_H) > 0. \tag{33}$$

6.3.2 Conservation of momentum

Definition and general force balance equations: Here, considering a surface with a basis of tangent vectors $\mathbf{e}_i$ and a normal vector $\mathbf{e}_n$, we recall that the force $\mathbf{f}$ on a line of length dl with unit vector $\boldsymbol{\nu} = \nu^i \mathbf{e}_i$, tangential to the surface of interest and normal to the line can be expressed as *(60)*.

$$\mathbf{f} = dl\nu^i \mathbf{t}_i = dl\nu_i \mathbf{t}^i, \tag{34}$$

where $\mathbf{t}_i$ is a tension that can be expressed into tangential and normal components

$$\mathbf{t}^i = t^{ij}\mathbf{e}_j + t^i_n \mathbf{e}_n. \tag{35}$$

In the absence of inertia, momentum conservation reduces to force balance. In the directions tangent to the surface, the force balance condition can be expressed as

$$\nabla_i t^{ij} + C^j_i t^i_n = (\sigma^{\text{oil}})^j_n - (\sigma^{\text{water}})^j_n. \tag{36}$$

Here, C_{ij} is the curvature tensor and $(\sigma^{\text{oil}})^j_n$ and $(\sigma^{\text{water}})^j_n$ are the normal-j components of the three-dimensonal stress tensor in the water and oil phases, respectively. In the direction normal to the surface, the force balance condition reads

$$\nabla_i t^i_n - C_{ij} t^{ij} = (\sigma^{\text{oil}})_{nn} - (\sigma^{\text{water}})_{nn}. \tag{37}$$

where $(\sigma^{\text{oil}})_{nn}$ and $(\sigma^{\text{water}})_{nn}$ are the normal-normal components of the three-dimensonal stress tensor in the water and oil phases, respectively. In the following, we will disregard the effects due to the shear in either the water or the oil interfaced and set the right-hand side of Eq. (36) to zero. In this case, $(\sigma^{\text{oil}})_{nn} - (\sigma^{\text{water}})_{nn} = \Delta P$, where ΔP is the pressure difference between the oil and the water phases. As argued in Sec. 6.2, we neglect the effects due to pressure difference within the oil droplet, and set $\Delta P = 0$ from now on.

The constitutive equations of a surface made of a growing nematic liquid crystal constrain the expression for the tension $\mathbf{t}^i$. Here, we consider that the in-plane components t^{ij} take the form

$$t^{ij} = -\zeta\Delta\mu g^{ij} - \tilde{\zeta}\Delta\mu(n^i n^j - g^{ij}/2) + \eta_b v^k_k g^{ij} + 2\eta\tilde{v}^{ij} + t^{ij}_e, \tag{38}$$

where $\zeta\Delta\mu$ and $\tilde{\zeta}\Delta\mu$ are the active stresses generated by the bacteria growth, with n^i the in-plane components of the cell orientation director field; $v_{ij} = (\nabla_i v_j + \nabla_j v_i)/2 + v_n C_{ij}$ is the velocity-gradient tensor and $\tilde{v}^{ij} = v^{ij} - v^k_k g^{ij}/2$ its traceless form; η_b and η are the bulk and shear viscous moduli; the equilibrium stress in Eq. (38) is defined as

$$t^{ij}_e = (f_e - \mu_b\rho)g^{ij} - K^{ik}C^j_k, \tag{39}$$

where f_e is the free-energy density associated to the biofilm deformation (e.g. the integrand in Eq. (15), $\mu_b = \partial f_e/\partial\rho$ is a chemical potential and $K^{ij} = \partial f_e/\partial C_{ij}$ is the passive bending moment. Furthermore, the normal component of the tension t^i_n takes the form

$$t^i_n = t^i_{e,n} = \nabla_j K^{ji}. \tag{40}$$

Application to the tube geometry: At the coordinates $\mathbf{r} = (r\cos(\theta), r\sin(\theta), z)$, the tangent vectors to the tube are $\mathbf{e}_z = \partial_z\mathbf{r}$ and $\mathbf{e}_\theta = \partial_\theta\mathbf{r}$; the unit normal vector is $\mathbf{e}_n = \mathbf{e}_\theta \times \mathbf{e}_z/|\mathbf{e}_\theta \times \mathbf{e}_z|$. From these expressions, the metric and curvature tensor are defined as $g_{ij} = e_i \cdot e_j$ and $C_{ij} = -(\partial_{ij}\mathbf{r}) \cdot \mathbf{e}_n$. The non-vanishing components of the previous tensors are: $g_{\theta\theta} = r^2$, $g_{zz} = 1$ and $C_{\theta\theta} = r$. Considering only states that are independent on the azimuthal coordinate θ and invariant along the axial coordinate z, Eqs. (38–40) take a simpler form. In particular, based on Eq. (15) with $\kappa_B = \kappa_{B,\perp}$, the non-vanishing components of the passive bending moment and the equilibrium in-plane tension read

$$K^{\theta\theta} = \left(\frac{1}{r} - C_{\theta,0}\right)\frac{\kappa_B}{r^2}, \tag{41}$$

$$t^{zz}_e = \left(\sigma(\rho) + \frac{\kappa_B}{2r^2} - \frac{\kappa_B C_{\theta,0}}{r}\right), \tag{42}$$

$$t^{\theta\theta}_e = \left(\sigma(\rho) - \frac{\kappa_B}{2r^2}\right)\frac{1}{r^2}, \tag{43}$$

where, considering the possibility of a density-dependent surface tension, we have

$$\sigma(\rho) = \gamma(\rho) - \frac{\partial \gamma(\rho)}{\partial \rho}\rho + \frac{\kappa_B C_{\theta,0}^2}{2}. \tag{44}$$

Note that $t_{e,n}^i = 0$. Besides, the non-vanishing components of the in-plane tension read

$$t^{zz} = \left(\sigma(\rho) - \bar{\zeta}\Delta\mu - \frac{\zeta\Delta\mu}{2} + \frac{\kappa_B}{2r^2} - \frac{\kappa_B C_{\theta,0}}{r}\right) + (\eta_b + \eta)v^{zz} + (\eta_b - \eta)\frac{v_n}{r}, \tag{45}$$

$$t^{\theta\theta} = \left(\sigma(\rho) - \bar{\zeta}\Delta\mu + \frac{\zeta\Delta\mu}{2} - \frac{\kappa_B}{2r^2} + (\eta_b - \eta)v^{zz} + (\eta_b + \eta)\frac{v_n}{r}\right)\frac{1}{r^2}. \tag{46}$$

Then, the force balance in the axial direction given by Eq. (36) implies that $t^{zz} = t_0^{zz} = cte$, where cte stands for a constant, and where t_0^{zz} represents an in-plane tension per unit length at the end of the tube. Due to the negligible pressure differences between the oil and water phases, the t_0^{zz} term vanishes. Similarly, force balance in the normal direction given by Eq. (37) implies that $rt^{\theta\theta} = 0$. Therefore, force balance entails that:

$$\sigma_{t,H} + \frac{\kappa_B}{2r^2} - \frac{C_{\theta,0}}{r}\kappa_B + (\eta_b + \tilde{\eta})\frac{\partial v_z}{\partial z} + (\eta_b - \tilde{\eta})\frac{1}{r}\frac{\partial r}{\partial t} = 0, \tag{47}$$

$$\sigma_{n,H} - \frac{\kappa_B}{2r^2} + (\eta_b - \tilde{\eta})\frac{\partial v_z}{\partial z} + (\eta_b + \tilde{\eta})\frac{1}{r}\frac{\partial r}{\partial t} = 0, \tag{48}$$

where we defined

$$\sigma_{t,H} = \sigma(\rho) - \zeta\Delta\mu - \tilde{\zeta}\Delta\mu/2, \quad \text{and} \quad \sigma_{n,H} = \sigma(\rho) - \zeta\Delta\mu + \tilde{\zeta}\Delta\mu/2. \tag{49}$$

Rapid normal stress equilibration: Here, we will assume that $\eta_b = \tilde{\eta}$, and that the tube radius remains constant at steady state; in this case, Eq. (48) reads

$$\sigma_{n,H} - \frac{\kappa_B}{2r_{\text{eq}}^2} = 0, \tag{50}$$

which sets the tube radius at

$$r_{\text{eq}} = \sqrt{\frac{\kappa_B}{2\sigma_{n,H}}}. \tag{51}$$

In this limit, Eq. (47) takes the expression:

$$\eta\frac{1}{L}\frac{dL}{dt} = -\left(\sigma_{t,H} + \sigma_{n,H} - \kappa_B\frac{C_{\theta,0}}{r_{\text{eq}}}\right), \tag{52}$$

where $\eta = \eta_b + \tilde{\eta}$; dL/dt is defined in Eq. (29). With all parameters being fixed, Eq. (52) predicts an exponential tube growth at a rate $-\kappa/\eta$, with

$$\kappa \equiv \sigma_{t,H} + \sigma_{n,H} - \kappa_B\frac{C_{\theta,0}}{r_{\text{eq}}}, \tag{53}$$

which corresponds to the Eq. (1) provided in the main text; tube formation then occurs when $\kappa < 0$. In the case $\sigma_{t,H} = \sigma_{n,H} = \gamma$, the expression in the left hand side of Eq. (53) is in line with the expression of the tube pulling force provided in Eq. (22).

Experimental estimates: We consider a bending energy of the order of $\kappa_B \approx Ew^3 = 10^{-12}\,\mathrm{N.m}$ *(61)*, with $E = 10^6\,\mathrm{Pa}$ and an estimated bacteria biofilm thickness $w = 10^{-6}$ m; an equilibrium tube radius of the form $r_{\mathrm{eq}} = 10^{-5}\,\mathrm{m}$ and a preferred radius $r_0 = 5 \cdot 10^{-6}\,\mathrm{m}$. This leads to a negative contribution to the overall effective surface tension $\kappa_{\mathrm{act}} \sim \kappa_B/(r_0 r_{\mathrm{eq}}) \sim 20\,\mathrm{mN.m}$, which is in the range of the measured surface tension values γ; we therefore expect the overall tension κ to be relatively small. Such conclusion is in line with the fact that the tube growth rate is relatively long, $\tau \approx 350\,\mathrm{min} \approx 10^4\,\mathrm{s}$ in experiments. Considering an effective, long-time *(62)*, two-dimensional biofilm layer viscosity $\eta = 1\ \mathrm{N.m^{-1}.s}$ (constructed as $\eta = \eta_{3\mathrm{D}} w$, with $\eta_{3\mathrm{D}} = 10^6\,\mathrm{N.m^{-2}.s}$ and $w = 10^{-6}\mathrm{m}$), we expect the total effective surface tension (estimated as $\kappa \sim \eta/\tau$) to be relatively small, in the $\kappa \sim 0.1\,\mathrm{mN.m}$ range.

Condition for tube formation: Solving for the condition $dL/dt = 0$ after substituting Eq. (50) into Eq. (52) yields the following critical equilibrium radius:

$$r'_{\mathrm{eq}} = \frac{\kappa_B C_{\theta,0}}{\sigma_{t,H} + \sigma_{n,H}}. \tag{54}$$

The condition $r'_{\mathrm{eq}} = r_{\mathrm{eq}}$ yields the critical surface tension condition:

$$\frac{(\sigma_{t,H} + \sigma_{n,H})^2}{2\sigma_{n,H}} < \kappa_B C_{\theta,0}^2. \tag{55}$$

In the case $\sigma_{t,H} = \sigma_{n,H} = \gamma$, this corresponds to Eq. (24).

In all the equations defined here in Sec. 6.3.2, there are no reference to the bacteria density field. This will be the subject of the next paragraph.

6.3.3 Coupling the stress equation to the bacterial density: oscillation analysis

Here, we show that the transition between the spherical and dendritic phenotypes – as well as the existence of oscillations between these phenotypes – is recapitulated through a relationship between the tube growth rate and the density of bacteria in the biofilm. We focus on the limit of a fast division rate, such that $\rho \approx \rho_{ss}(\dot{L})$, where $\rho_{ss} = 1 - \dot{\epsilon}/k_d$ is the

steady-state density defined in Eq. (32), with $\dot{\epsilon} = \dot{L}/L$. The tube growth rate defined in Eqs. (52) and (53) can then be expressed as:

$$\eta\dot{\epsilon} = -\kappa(\rho), \tag{56}$$

where we now assume that the tube growth rate κ is coupled to the local density ρ; we approximate such coupling to its second order expansion around ρ_{ss}:

$$\kappa \sim k_0 - k_1\rho + k_2\rho^2. \tag{57}$$

The expansion in ρ in Eq. (57) could specifically originate from the active stress contribution $\sigma_{t,H}$ in Eq. (52).

6.3.4 Oscillations

With $\rho_{ss} = 1 - \tau\dot{\epsilon}$, expanding Eq. (57) at first orders in the tube growth rate $\dot{\epsilon}$ then leads to

$$\kappa \sim \hat{k}_0 - \hat{k}_1\tau\dot{\epsilon} + \hat{k}_2\tau^2\dot{\epsilon}^2, \tag{58}$$

where $\hat{k}_0 = k_0 - k_1\rho_H + k_2\rho_H^2$, $\hat{k}_1 = k_1 - 2k_2\rho_H$, $\hat{k}_2 = k_2 > 0$. Given Eq. (58), there can be two stable solutions to Eq. (56), one corresponding to a collapsing velocity $\dot{\epsilon}_c < 0$ and the other corresponding to a growth velocity $\dot{\epsilon}_g > 0$. Processes limiting the growth or collapse of the biofilm length can trigger a switch between these two stable solutions: (1) a progressive increase in the oil pressure, as predicted by Laplace law Eq. (19) with $R_d \to 0$, could trigger a transition from the growth phase to the collapse phase; (2) such collapse phase eventually stops when the total interface length reaches the minimal critical value set by the quantity of oil within the droplet, triggering the onset of a new growth phase. Such oscillation mechanism is reminiscent of the one proposed to describe molecular motors assemblies *(41)*.

In the next section, we propose a phase-field model in which oscillations between the spherical and dendritic phenotype emerge spontaneously, following an analogous mechanism to the one described above.

7 Phase-field model for the spherical-dendritic oscillations

7.1 Shape of the oil droplet: a Phase-field model

Here, we propose a Phase-field model to account for the evolution in the shape of the oil droplet. In such model, a field ϕ models the local relative fraction in oil, with $\phi = 1$

within the oil droplet and $\phi = 0$ elsewhere. For simplicity, we focus on a two-dimensional configuration with periodic boundary conditions; we consider an initially circular droplet of radius R (see Sec. 7.5 for more details).

7.1.1 Model description

In the absence of oil consumption, we consider a Cahn-Hilliard-like equation:

$$\frac{\partial \phi}{\partial t} = M \nabla^2 \mu_\phi, \tag{59}$$

where $M > 0$ is a diffusion coefficient, and

$$\mu_\phi = \frac{\delta \mathcal{F}_{CH}}{\delta \phi}, \tag{60}$$

is a chemical potential defined in terms of a Canham-Helfrich free energy

$$\mathcal{F}_{CH} = \int \mathrm{d}^2\mathbf{r} \left\{ \frac{1}{2} a \phi^2 (1-\phi)^2 + \frac{1}{2} \kappa_1 (\nabla \phi)^2 + \frac{1}{2} \kappa_2 \left(\nabla^2 \phi \right)^2 \right\}. \tag{61}$$

In two-dimension, the term κ_1 corresponds to an effective surface tension; κ_2 corresponds to a Helfrich energy; the ratio of the parameters a and κ_2 control the width of the oil/water interface, which scales as $\ell \sim (\kappa_2/a)^{1/4}$. We choose a set of parameters such that the length of the interface remains sharp.

7.1.2 Model results

We first simulated the behavior of Eq. (59) varying the value of $-\kappa_1$ with all other parameters fixed at the values defined in Sec. 7.5. As illustrated in fig. S15, we find that digitation (representing tubes) are observed only for sufficiently negative values of the effective surface tension

$$\kappa_1 < \kappa_{c,1} \approx -0.75. \tag{62}$$

7.2 Bacterial population at the oil-water interface: a logistic growth model

We now model the bacterial population growth. Following Eq. (31), we consider that number of bacteria within the interface N follows a logistic growth *(62)*:

$$\frac{dN}{dt} = N k_d (1 - \rho/\rho_H), \tag{63}$$

where the density ρ is defined as

$$\rho(t) = N(t)/\mathscr{L}(t), \tag{64}$$

where, following Ref. *(63)*, we consider the following measure for the oil-water interface length

$$\mathscr{L}(t) = \int \mathrm{d}^2\mathbf{r}|\nabla\phi|. \tag{65}$$

7.3 Modulation of the oil surface tension by the bacteria density

Inspired by Eqs. (26) and (57), we consider the interfacial term defined in Eq. (61) to read:

$$\kappa_1(\rho) = k_0 - k_1\rho + k_2\rho^2 = k_2(\rho - \rho_1)(\rho - \rho_2). \tag{66}$$

Solving for $\kappa_1(\rho_1) = \kappa_{c,1}$, as defined in Eq. (62), yields two critical densities

$$\rho_1 = \frac{k_1 - \sqrt{k_1^2 - 4\tilde{k}_0 k_2}}{2k_2}, \qquad \text{and} \qquad \rho_2 = \frac{\sqrt{k_1^2 - 4\tilde{k}_0 k_2} + k_1}{2k_2}, \tag{67}$$

with $\tilde{k}_0 = k_0 - \kappa_{c,1}$; these are positive when $k_1^2 - 4\tilde{k}_0 k_2 > 0$ and $k_1, k_2 > 0$. As discussed in Sec. 7.1 and fig. S15, tubes form for any constant value of the density ρ in the range (ρ_1, ρ_2), since $\kappa_1(\rho_1) < \kappa_{c,1}$.

We then turn to simulations where Eq. (63) is implemented together with the coupling Eq. (66). Different regimes appear according to the value of the homeostatic density ρ_H with respect to ρ_1, ρ_2 and the density minimizing $\kappa_1(\rho)$, denoted as ρ_S, which reads

$$\rho_S = k_1/(2k_2). \tag{68}$$

Starting with a spherical droplet (SB) with $\rho = 0.001$ at $t = 0$, the droplet either

1. (for $\rho_1 < \rho_H < \rho_S < \rho_2$) evolves into a stable dendrite structure, see movie S4. This behavior mimics the dendritic phenotype observed for long culture time.

2. (for $\rho_1 < \rho_S < \rho_H < \rho_2$) exhibits sustained oscillations between a spherical and a dendritic structure, see fig. S16 and movie S4. This behavior mimics the oscillatory behavior observed in experiments at intermediate culture time.

3. (for $\rho_H < \rho_1$) remains spherical, see movie S4. This behavior mimics the spherical phenotype observed for short culture time.

4. (for $\rho_H > \rho_2$) first evolves into a dendritic structure that eventually collapses back into a sphere.

This set of behavior is recapitulated in the phase diagram of fig. S17.

7.4 Relating the phase-field model to the membrane model of Sec. 6.3

Relating κ_1 (phase-field model) to κ (membrane model): Tube form in the phase-field model whenever κ_1 is lower than a threshold value $\kappa_1 < \kappa_{c,1}$, see fig. S15. We identify the condition $\kappa_1 < \kappa_{c,1}$ to the condition $\kappa < 0$ set in Eq. (56). As shown in fig. S15, in the range $\kappa_{c,1} < \kappa_1 \in (-0.8, -0.95)$, the rate of growth in the interface length, denoted $\dot{\mathscr{L}}/\mathscr{L}$, increases linearly with $-\kappa_1$, which mimics the behavior of $\dot{L}/L$ described in Eq. (56).

Relating M (phase-field model) to η (membrane model): The time-scale unit in Eq. (61) is set by the parameter M while, in the continuum membrane model Eq. (38), it is set by $\eta = \eta_b + \tilde{\eta}$.

Relating the growth rate k_d (phase-field model) to τ (membrane model): Expressing the time derivative of Eq. (64) in terms of Eq. (63), we obtain a relation analogous to Eq. (30), with $k_d = 1/(\rho_H \tau)$.

Relating κ_2 (phase-field model) to κ_B (membrane model): For the set of parameters corresponding to the dendritic phenotype model (case 1, page 28), we find that the thickness of individual fingers scales as $\ell \sim (\kappa_2/a)^{1/4}$; we therefore map the interface thickness to the tube radius defined Eq. (51), $\ell \sim r_{\mathrm{eq}} = \sqrt{\kappa_B/(2\sigma_{n,H})}$.

7.5 Numerical implementation

We employ a finite difference method to solve Eqs. (59) and (63). The time integration is performed using a backward Euler scheme; the spatial derivatives are carried out using a second-order central difference. Simulations were performed on a 256 × 256 two-dimensional lattice using periodic boundary conditions. The system was initialized with a circular shape of oil of radius R centered within the simulation domain, that is $\phi = 1$ for $r = \sqrt{x^2 + y^2} \leq R$ and $\phi = 0$ elsewhere.

If not considered otherwise, we consider the following parameter values: $a = 10$, $M = 0.5$, $\kappa_2 = 0.1$, $k_d = 0.1$, $k_0 = 1.35$, $k_2 = 3.0$, $R = 5$, $\Delta x = 0.125$, $\Delta t = 0.001$. The other parameter values (which are recalled in the movie S4 caption) read

- for the SB phenotype: $k_1 = 5.0$, $\rho_H = 1.2$.
- for the OB phenotype: $k_1 = 5.4$, $\rho_H = 1.2$.
- for the DB phenotype: $k_1 = 5.4$, $\rho_H = 1$.

7.6 Model extensions

7.6.1 Including fluctuations

Fluctuations in the droplet shape can be considered through a conservative fluctuating current term, denoted $\vec{J}$

$$\frac{\partial \phi}{\partial t} = M\nabla \cdot \left[\nabla \mu_\phi + \vec{J}\right], \tag{69}$$

where $\vec{J}$ is a fluctuating Gaussian white noise vector, with zero mean and correlations

$$\langle J_i(\boldsymbol{x}, t) J_j(\boldsymbol{x}', t')\rangle = \Sigma^2 \delta(\boldsymbol{x} - \boldsymbol{x}')\delta(t - t')\delta_{ij}. \tag{70}$$

In movie S4, we considered a simulation with $\Sigma = 0.05$. Stable oscillations occur even in the presence of a high level of interfacial fluctuations, showing the robustness of the proposed mechanism.

7.6.2 Including oil consumption

We have not considered the effect of oil consumption by the biofilm. The quantity μ_ϕ defined in Eq. (60) is indeed a Lagrange multiplier that conserves the integrated value of ϕ. Oil consumption by the biofilm could be investigated by considering the following expression for the oil droplet evolution equation:

$$\frac{\partial \phi}{\partial t} = M\nabla^2 \mu_\phi - k_c|\nabla \phi|, \tag{71}$$

such that $k_c > 0$ corresponds to the rate of oil consumption. We leave the impact of oil consumption to further studies.

8 Fit of the topological-defects mediated dimple profiles

In the following, we aim at estimating the parameters of our membrane model from experimental data – namely, from the height profiles around aster topological defects observed in the flattened biofilms experiment, see Fig. 4D and fig. S10.

8.1 Derivation of the fitting formula

We first provide a derivation of the linearized shape equation based on Ref. *(29)*. For more details on the theoretical framework and derivation of the nonlinear shape equation, we refer to Refs. *(29,42)*.

8.1.1 Disk geometry

To model the experimental observation of dimple formation near aster topological defects as described in Fig. 4, we consider a flat circular domain of radius R (called R_{dimple} in the main text) that represents the edge of the visible droplet. Following the observation of fig. S10, the bacterial orientation is represented by a fixed director field $\mathbf{n}$ along the radial direction $\mathbf{e}_r$ and with modulus $|\mathbf{n}| = 1$. The biofilm surface is parameterized by the position vector $\mathbf{r} = (r\cos(\theta), r\sin(\theta), h(r))$, where $h(r)/R \ll 1$ and $h'(r) \ll 1$. The corresponding basis of tangent vectors are: $\mathbf{e}_r = \partial_r \mathbf{r} = (\cos(\theta), \sin(\theta), h'(r))$ and $\mathbf{e}_\theta = r(-\sin(\theta), \cos(\theta), 0)$ and $\mathbf{e}_n = (-h'(r)\cos(\theta), -h'(r)\sin(\theta), 1)/\sqrt{1+h'(r)^2}$ is the unit vector normal to the surface. With these notations, the elementary surface area defined in Eq. (15) reads $da = drd\theta\sqrt{\det(g_{ij})}$ where $\det(g_{ij})$ is the determinant of the metric tensor. The non-vanishing components of the metric tensor $g_{ij} = \mathbf{e}_i \cdot \mathbf{e}_j$ are $g_{rr} = 1 + h'(r)^2$ and $g_{\theta\theta} = r^2$, leading to $\det(g_{ij}) = (1+h'(r)^2)r^2$. The non-vanishing components of the curvature tensor $C_{ij} = -(\partial_{ij}\mathbf{r}) \cdot \mathbf{e}_n$ are $C_{rr} = -h''(r)/\sqrt{1+h'(r)^2}$ and $C_{\theta\theta} = -rh'(r)/\sqrt{1+h'(r)^2}$. This leads to the expression of the squared mean curvature

$$\left(C_r^r + C_\theta^\theta\right)^2 \sim \left(-h''(r) - \frac{1}{r^2} \times rh'(r)\right)^2, \tag{72}$$

where we have used that $g_{rr} \sim 1$ at leading order in $h' \ll 1$.

8.1.2 Result

We consider the free energy of Eq. (15) with $\kappa_{B,\parallel} = \kappa_{B,\perp} = \kappa_B/2$. We set for simplicity that $C_{0,\perp} = C_{\parallel,0} = 0$; this amounts to supposing that at the early stage of the dimple

formation considered here, the effect of the spontaneous curvature C_0 is not apparent. The term $C_\perp^2 + C_\parallel^2$ is replaced by the squared mean curvature Eq. (72). In this context, at leading order in the perturbations $h/R, h' \ll 1$ the free energy expression Eq. (15) reduces to:

$$\mathcal{F} \approx \int dr d\theta \left\{ \gamma r \left(1 + \frac{h'(r)^2}{2}\right) + \frac{\kappa_B}{4} r \left(h'' + \frac{h'}{r}\right)^2 + \frac{\kappa_F}{2r}\left(1 - \frac{h'(r)^2}{2}\right)\right\}. \tag{73}$$

The minimal steady-state $h(r)$ profiles satisfy the condition $\delta\mathcal{F}/\delta h = 0$, which reads as

$$-\frac{\gamma}{r}\partial_r\left(r\partial_r h\right) + \frac{\kappa_B}{2r}\partial_r\left(r\partial_r\left(\frac{1}{r}\partial_r\left(r\partial_r h\right)\right)\right) + \frac{\kappa_F}{2r}\partial_r\left(\frac{\partial_r h}{r}\right) = 0. \tag{74}$$

This equation is, to linear order, the shape equation of a membrane with nematic order and an aster topological defect at $r = 0$ *(42)*. Integrating Eq. (74) with respect to the radial coordinate r and enforcing the integration constant to vanish, one obtains:

$$-\gamma r\partial_r h + \frac{\kappa_B}{2}\left(r\partial_r\left(\frac{1}{r}\partial_r\left(r\partial_r h\right)\right)\right) + \frac{\kappa_F}{2}\left(\frac{\partial_r h}{r}\right) = 0. \tag{75}$$

The latter equation has a simple solution:

$$\partial_r h = A_1 I\left(\sqrt{1-\frac{\kappa_F}{\kappa_B}}, \frac{r}{\sqrt{\kappa_B/2\gamma}}\right) + A_2 K\left(\sqrt{1-\frac{\kappa_F}{\kappa_B}}, \frac{r}{\sqrt{\kappa_B/2\gamma}}\right), \tag{76}$$

where $I(\alpha, x)$ and $K(\alpha, x)$ are Modified Bessel Functions of order α and both A_1 and A_2 are integration constants. The boundary condition $h(r = R) = 0$ leads to $A_1 = 0$, as $I(\alpha, x)$ diverges when $x \to \infty$; the boundary condition $h(r = 0) = h_0$ then determines the value of A_2. After a change of variable from r to $z = r/R$, we derive the following expression for the height profile near an aster topological defect

$$h(r) = h_0 \frac{\int_1^{r/R} K\left(\sqrt{1-\frac{\alpha_2}{\alpha_1}}, \frac{z}{\sqrt{\alpha_1}}\right) dz}{\int_1^0 K\left(\sqrt{1-\frac{\alpha_2}{\alpha_1}}, \frac{z}{\sqrt{\alpha_1}}\right) dz}, \tag{77}$$

expressed in terms of the following dimensionless constants

$$\alpha_1 = \kappa_B/(2\gamma R^2), \quad \text{and} \quad \alpha_2 = \kappa_F/(2\gamma R^2). \tag{78}$$

8.1.3 Discussion

In Ref. *(42)*, Eq. (74) was generalized for a membrane with an active nematic liquid crystal, and the authors found that the anisotropic active stresses renormalized the

surface tension γ and the elastic constant κ_F in a space-dependent manner. In the experiments considered here, we do not observe significant motility of the defects during the dimple formation process, hence we neglected the effects of anisotropic active stresses to explain the dimple formation.

8.2 Fitting procedure

We seek to evaluate the goodness-of-fit of Eq. (77). We analyze time-lapse images from n=6 flattened oil droplets. For each experiments and for each time point, we estimate the following error function for a large set of parameters $(\alpha_0, \alpha_1, \alpha_2)$

$$\mathcal{E}(\alpha_0, \alpha_1, \alpha_2) = \sqrt{\sum_{n=1}^{4} \sum_{r_i} |h^{\rm exp}(r_i) - h^{\rm fit}(r_i; (\alpha_0, \alpha_1, \alpha_2))|^2}, \tag{79}$$

where

- $r_i = i\Delta r$, with $i = 1, \ldots, 200$, is a radial set of coordinates, computed with respect to the position of the maximal peak; in the following we consider a radial step $\Delta r = 0.005R$ (corresponding to $\Delta r \approx 0.13$ μm).
- $h^{\rm exp}$ corresponds to the experimental value of the dimple height at the radial position r_i, after (1) normalization by its value at $r_1 = \Delta r = 0.005R$ and (2) removing an offset; the offset was the averaged height at large distances from the position of the maximal peak, a region of $10 - 15$ μm below R.
- $h^{\rm fit}$ is the fitting function, defined as

$$h^{\rm fit}(r; (\alpha_0, \alpha_1, \alpha_2)) = \alpha_0 \frac{\int_1^{r/R} K\left(\sqrt{1 - \frac{\alpha_2}{\alpha_1}}, \frac{z}{\sqrt{\alpha_1}}\right) dz}{\int_1^{r_1/R} K\left(\sqrt{1 - \frac{\alpha_2}{\alpha_1}}, \frac{z}{\sqrt{\alpha_1}}\right) dz}, \tag{80}$$

  which corresponds to the theoretical expression of Eq. (77); given our normalization choice, we expect that $\alpha_0 \approx 1$.
- the sum in Eq. (79) runs over all experimental position r_i at a given instant of time and over $n = 4$ radial cuts profiles, which are chosen along perpendicular planes crossing the center of the oil droplet.

For a given droplet, profiles at different time points are grouped by the value of their maximal height. For the data set that was analyzed, the dimple radius ranges from $R = 25 - 35$ μm and the height of dimples ranges from $4 - 8$ μm.

The error function $\mathcal{E}$ of Eq. (79) was computed in the parameter space $(\alpha_0, \alpha_1, \alpha_2) = (10^{-1}, 10) \times (1, 10^4) \times (1, 10^4)$. To locate the absolute minimum $\mathcal{E}_{\min}$, we constructed fig. S11, which shows the subset of the previous parameter space whereby the error function $\mathcal{E} < 1.2 * \mathcal{E}_{\min}$. Our analysis disclosed regions of the parameter space that are compatible with the experimental measurements: fig. S11 - fig. S12 shows the averaged theoretical fits for each independent experiment. To compute the fitting parameters from table S2, we used the regions of parameters from fig. S11 and found that the ratio κ_F/κ_B is bounded in most of the experimental cases to a value below 5.5 and in some cases it is constrained to an average value between $1.7 - 2.0$. In all experimental cases, the averaged value of α_0 is close to 1, as expected. In one experimental case, we compared experimental profiles with a height < 6 μm and > 6 μm (fig. S12) and found no differences in the parameter values $\kappa_B/\gamma R^2$ and $\kappa_F/\gamma R^2$ (fig. S12a and table S2).

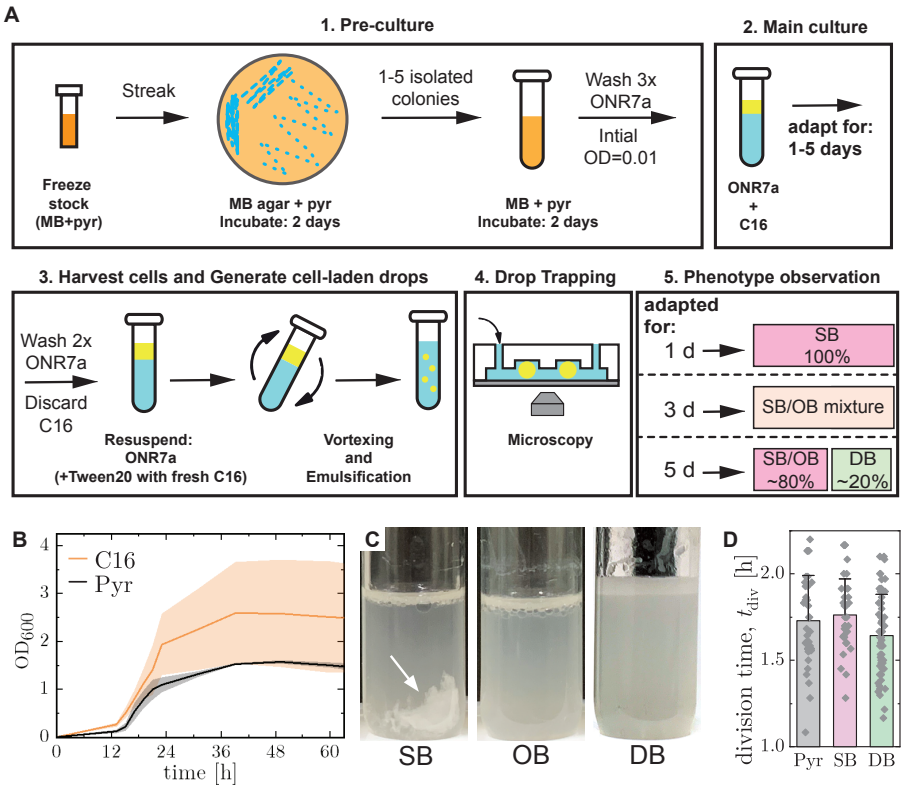

Fig. S1: Culture method schematic describing phenotype identification. (A) Diagram outlining the: 1) pre-culture process; 2) main culture and adaptation of *A. borkumensis* to growth using C16; 3) cell harvesting and generation of cell-laden drops with fresh C16; 4) microfluidic drop trapping and imaging; and 5) identification of biofilm phenotype using microfluidics. (B) Growth curves of *A. borkumensis* grown in ONR7A media supplemented with C16 or pyruvate (Pyr), respectively. Solid lines and shaded regions represent the mean $\pm$ SD from three separate experiments. (C) Images of typical test tube cultures, taken after 5 d of cultivation prior to phenotype determination. The SB phenotype often develops a sedimented biofilm (see arrow). The OB phenotype tends to lack the sedimented biofilm but has emulsion droplets similar to the SB. The DB phenotype tends to be more turbid than the other two, lacks the sedimented biofilm, and has smaller emulsions than the other two. (D) The average division time (t_{div}) of cells grown on Pyr (n=37; 2 independent tests), SB-forming cells grown on C16 (n=36 cells; 3 independent tests), and DB-forming cells grown on C16 (n=61 cells; 5 independent tests), respectively.

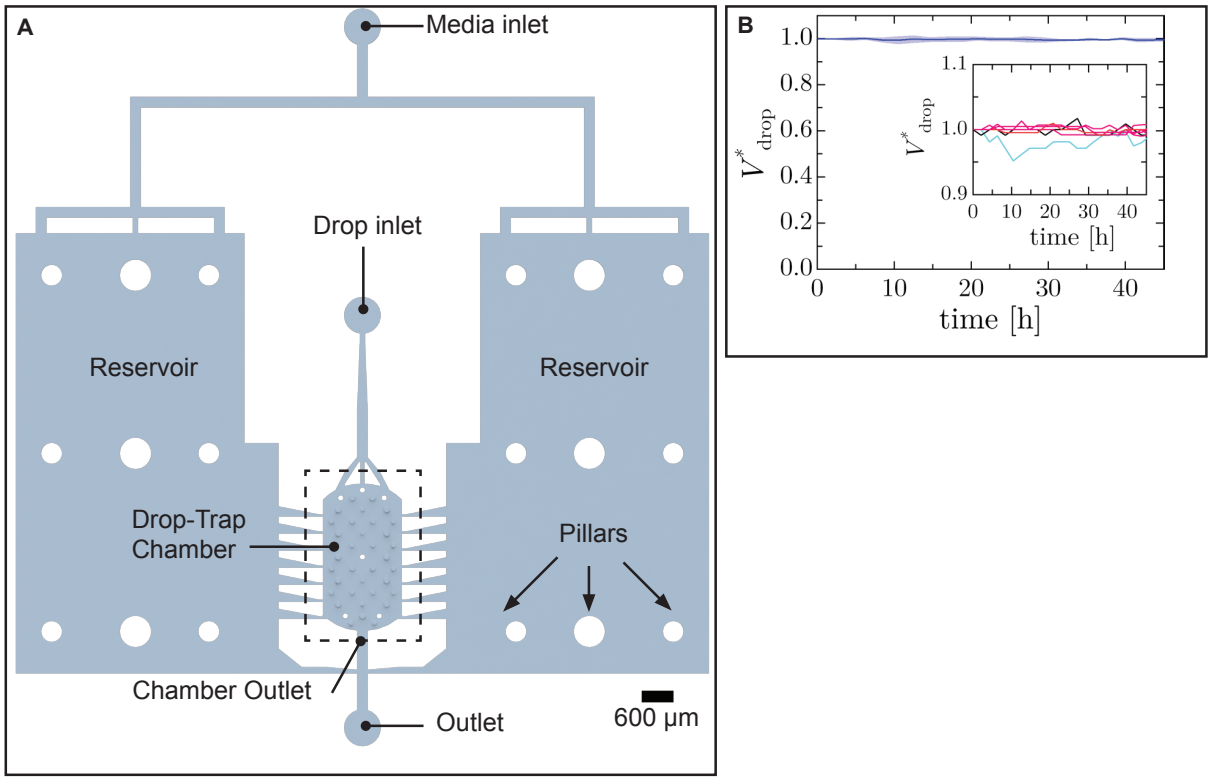

Fig. S2: Microfluidic device design. (A) Schematic of the 2-layer microfluidic oil-drop trap device used in these experiments. The media-filled channels are shown. The dashed line indicates the drop-trap chamber, which is shown in Fig. 1A. The white circles are pillars and small 'raised' blue circles are the drop traps. The media inlet connects to reservoirs that provide a gentle flow through the trap chamber. The drop inlet port is used only to introduce the cell-laden drops into the device. (B) Normalized volume of trapped oil drops over time. Devices are coated with PVA to prevent absorption of C16 by the PDMS channels, which have been measured to suppress absorption for at least 21 days. The solid line and filled area represent the mean $\pm$ SD (n = 15 drops). (inset) Magnified view of the individual experiments.

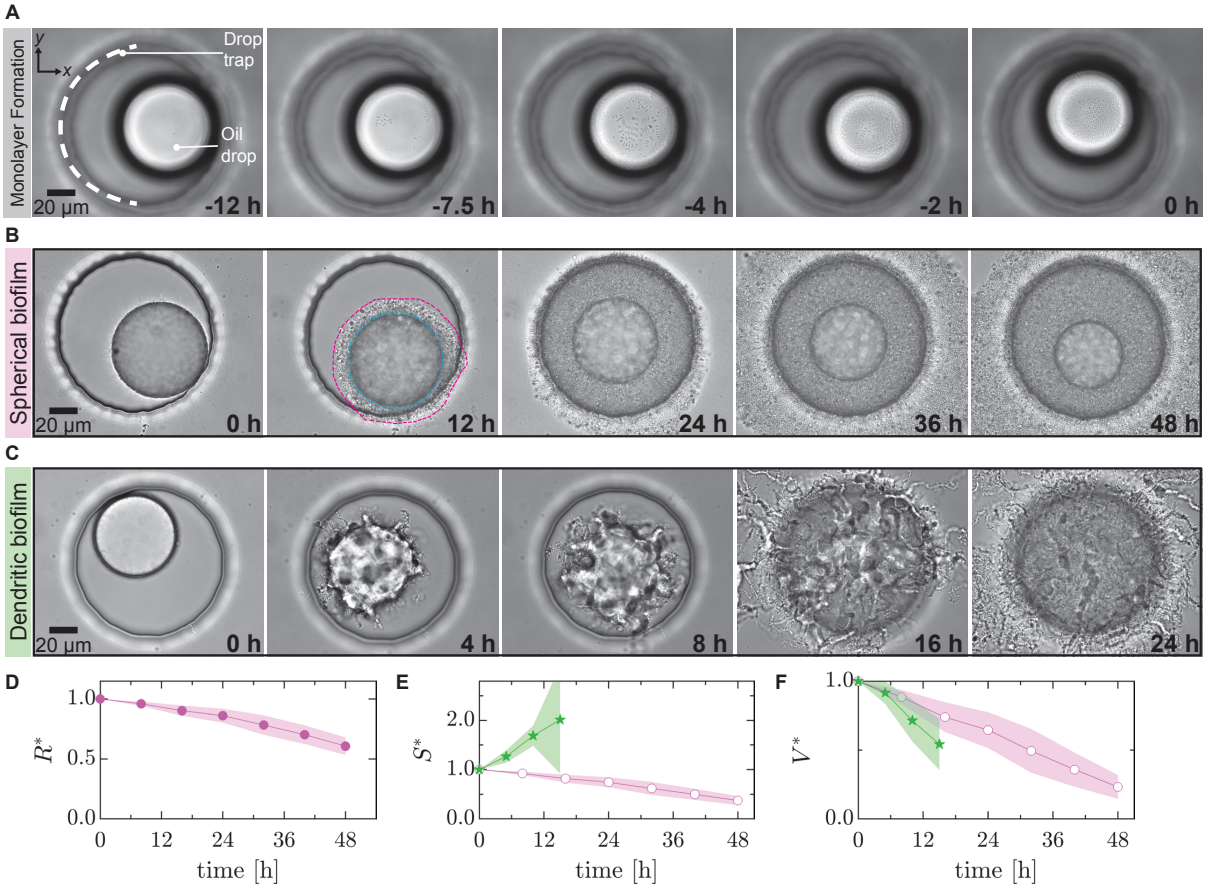

Fig. S3: Bright-field sequences showing biofilm phenotypes. (A) Time-lapse sequence showing the formation of a monolayer on a trapped drop. The edge of the drop trap is indicated by the white dashed line. The confluent monolayer is formed at t_0 (t = 0 h). (B) Development of a spherical biofilm (SB) on an oil drop. The oil drop radius monotonically decreases in time. At 12 h, the droplet is outlined with a cyan line and the biofilm is outlined by a magenta line, as a guide for the reader. (C) Time-lapse sequence showing the development of a dendritic biofilm (DB) on an oil drop. The biofilm deforms the surface, initially generating wrinkles and protrusions, that fragmenting the droplet into tube-like segments and numerous smaller irregularly shaped volumes of oil covered with cells at later times. (D) Normalized radius ($R^* = R/R_0$); (E) normalized surface area ($S^* = S/S_0$); and (F) normalized volume ($V^* = V/V_0$) of oil drops as a function of time for (•) SBs and ($\star$) DBs (solid lines and filled regions: mean ± SD; $\mathrm{n_{SB}}$ = 10 drops; $\mathrm{n_{DB}}$ = 10 drops; representative data from a test independent of data in Fig. 1D,E). The unfilled symbols in (E) and (F) are calculated from R^* in (D).

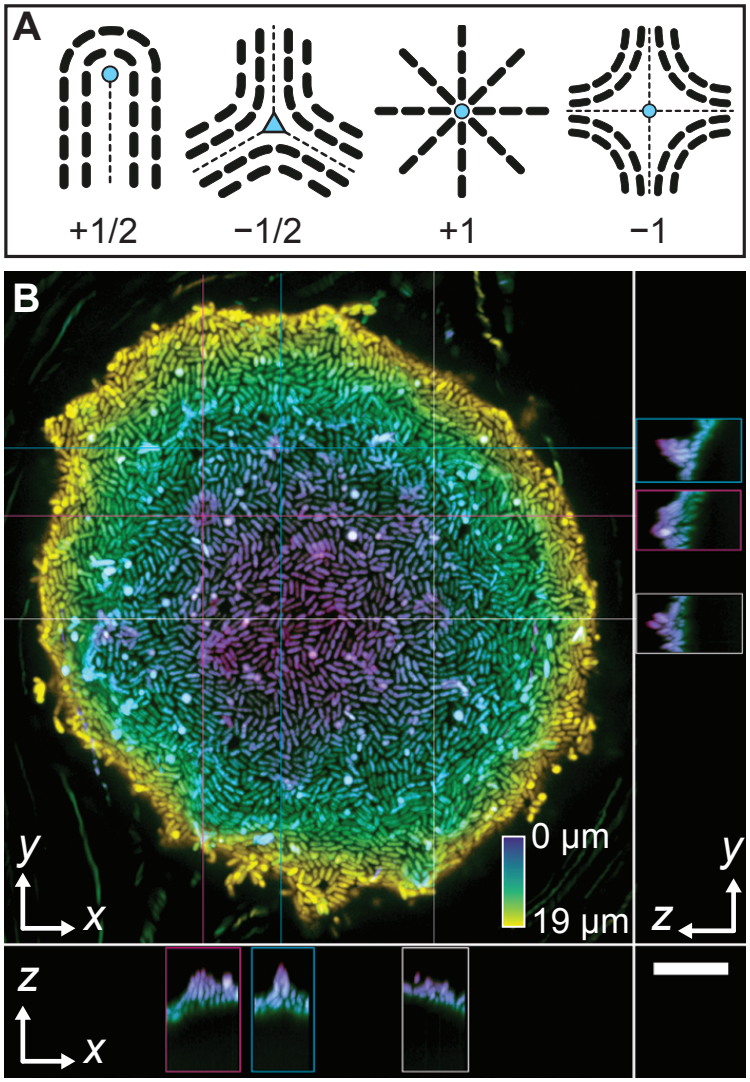

Fig. S4: Confocal image of a biofilm presenting nematic topological defects. (A) Schematic of nematic defects with charges of $\pm 1/2$ and ± 1 observed in our system. (B) Maximum intensity projection confocal image of a droplet at $\sim$ 10 h into biofilm development. The colored cross-hairs intersect different +1 topological defects, shown in the orthogonal planes, below and to the right. Scale bar = 10 μm. The image is color coded by depth with the colormap scale ranging from 0-19 μm.

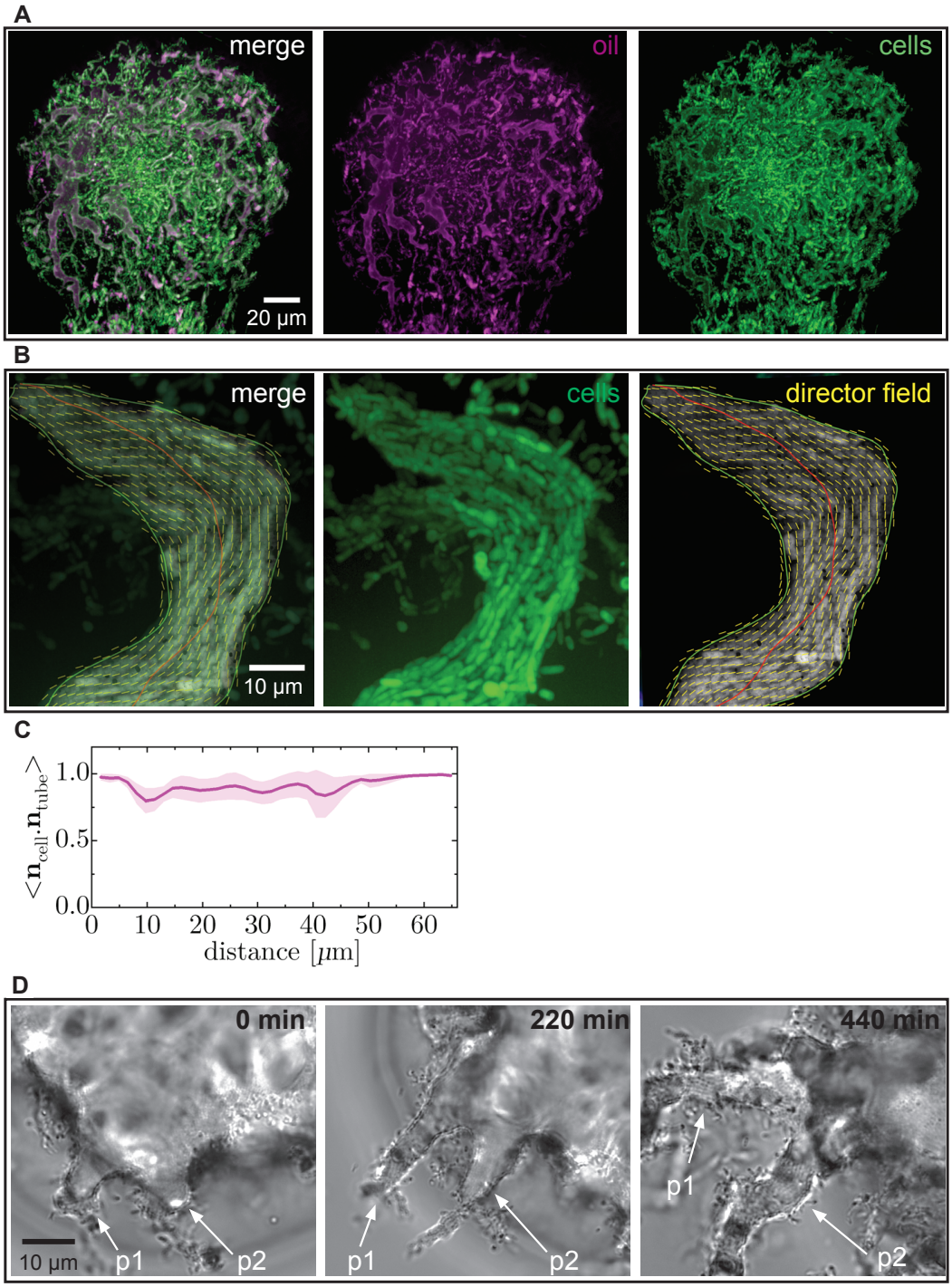

Fig. S5: (Caption next page.)

Fig. S5: Cell-stabilized oil filled tubes. (A) A merged 2-color confocal image of an oil drop in the later stages ($\sim$15 h) of deformation by a DB. FM-464 ($\lambda_{\mathrm{ex}}/\lambda_{\mathrm{em}}$ = 515 nm/640 nm) is a hydrophobic dye added to the media at a concentration of 2 μM to label the oil. The bacteria constitutively express EGFP ($\lambda_{\mathrm{ex}}/\lambda_{\mathrm{em}}$ = 488 nm/509 nm). The co-localization of magenta and green indicates that the dendritic branches are bacteria-stabilized tubes containing oil. (B) Confocal image of a bacteria-covered oil tube with the orientation director field overlaid. The red line in the director field is the central axis of the tube. (C) Dot product calculated for (B) between the cell axis and the tube axis (red) averaged over all cells in bin widths of 1.45 μm. Solid line and shaded regions represent mean $\pm$ SD. (D) Image sequence showing the evolution of representative tubes. Due to rotation of the mother droplet, the location of the two protrusions, p1 and p2, respectively, rotate clockwise in subsequent frames.

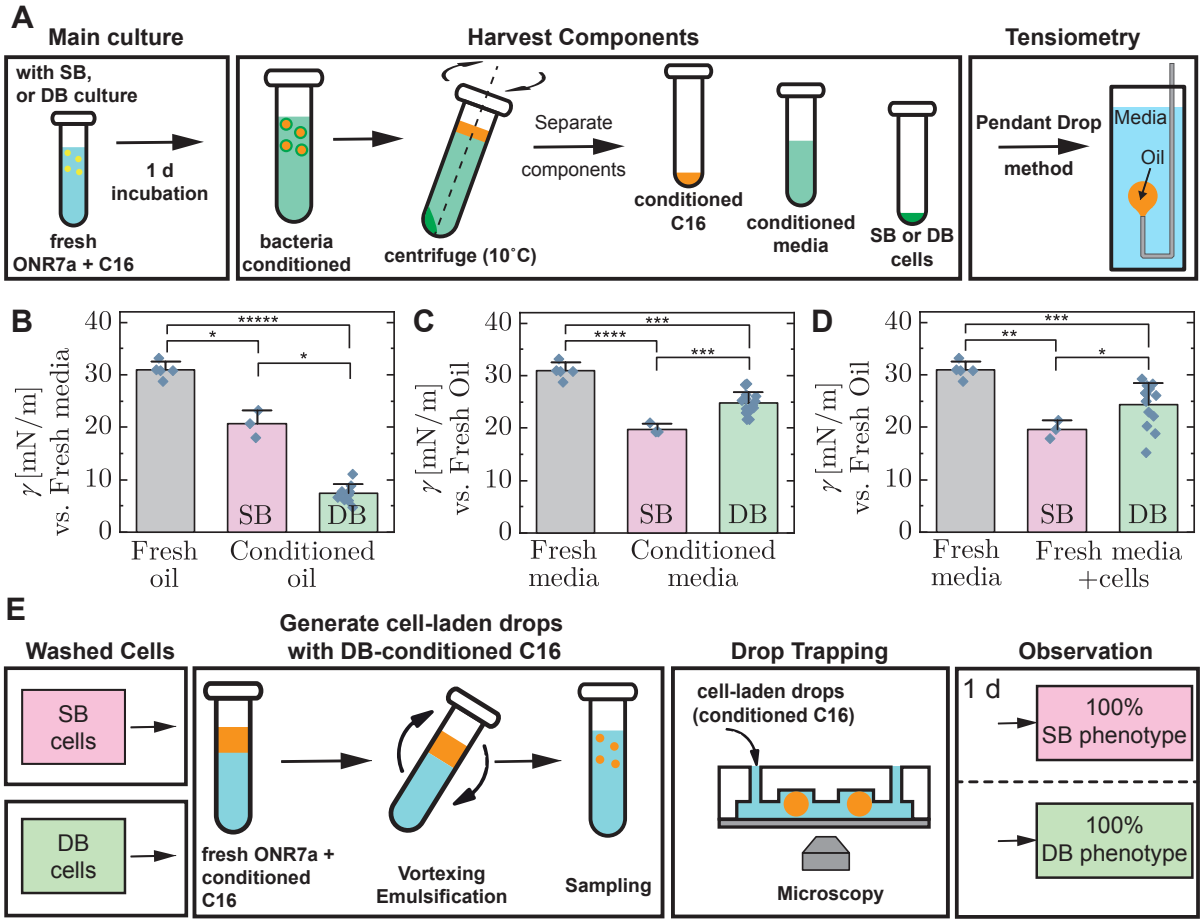

Fig. S6: (Caption next page.)

Fig. S6: Interfacial tension measurements of the bacteria-conditioned components from liquid culture. (A) Schematic summarizing the separation and harvesting of each conditioned component of the liquid cultures and the interfacial tension (γ) measurements for SB and DB cultures (see Sec. 1 and 2.5 for culture preparation). The detailed method is described in methods Sec. 3.1. (B) γ for conditioned C16 against fresh media (mean + SD. $n_{control}$=5; n_{SB}=3; n_{DB}=10; each measurement was done independently). This data, which is shown in Fig. 2C, is reproduced here to facilitate comparison. (C) γ for conditioned media against fresh C16 (mean + SD. $n_{control}$=5; n_{SB}=3; n_{DB}=14; each measurement was done independently). The conditioned media was filtered through a 0.22 μm filter to remove all cells. (D) γ for fresh media containing harvested cells that were washed (3x) after 1 day of culture against fresh C16 (mean + SD. $n_{control}$=5; n_{SB}=3; n_{DB}=14; each measurement was done independently). In (B-D) asterisks indicate statistical significance: *: $p < 0.05$; **: $p < 0.01$; ***: $p< 0.001$; ****: $p< 10^{-4}$; *****: $p< 10^{-5}$; p value, Welch's t-test with Holm-Bonferroni correction. (E) Schematic describing the method we used to measure the phenotypic outcome from microfluidic sampling when we use conditioned oil as the substrate instead of fresh oil. Conditioned oil was obtained from a DB liquid culture incubated for $\sim$20 h (see (A) and methods Sec. 2.5). Here $\gamma \simeq$ 8 mN/m (see (B)). The observed phenotype remains constant despite using conditioned oil (n_{SB}= 6; n_{DB}=3; each measurement was done independently).

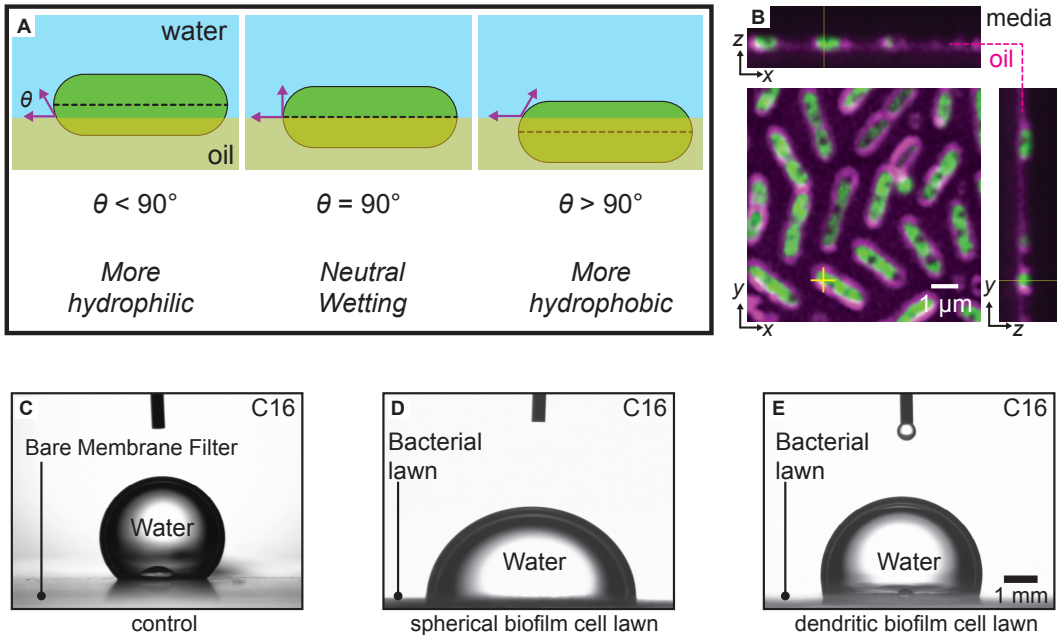

Fig. S7: C16 wettability of the cell surface. (A) Schematic showing how spherocylinders of different surface-hydrophobicity will sit at the oil-water interface at equilibrium. (B) Confocal image of GFP-expressing DB cells at a flat oil-water interface that have been labeled with FM-464 (magenta). In addition to the cell membrane, FM-464 also stains the oil and can be used to visualize the water-oil interface (see faint magenta line in the orthogonal planes). The cells appear to have near neutral wetting. See Microfluidics Methods for experimental details. (C-E) Representative images of a 3-phase contact angle test for a water droplet submerged in C16 in contact with: (C) the bare membrane filter ($\theta = 133 \pm 5°$ (mean±SD)); (D) the filter membrane supporting a bacterial lawn consisting of SB cells ($\theta = 80 \pm 8°$); and (E) the filter membrane supporting a bacterial lawn of DB cells ($\theta = 110 \pm 10°$).

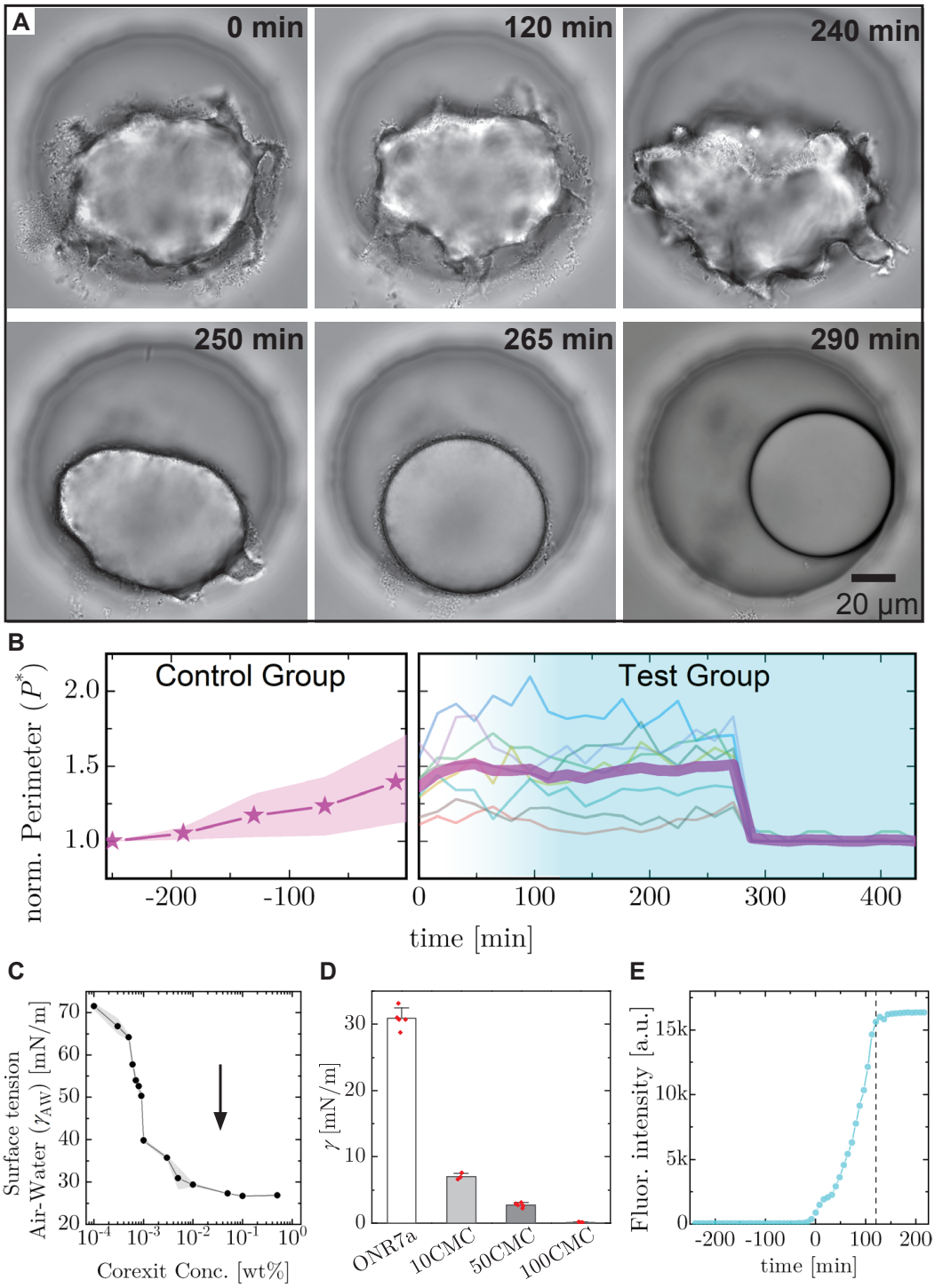

Fig. S8: (Caption next page.)

Fig. S8: Surfactant mixture disrupts DBs on oil drops. (A) Time-lapse sequence showing the effect of a surfactant mixture (mock Corexit) on a typical dendritic biofilm (DB). Media containing 1× the critical micelle concentration (CMC) is infused into the device, taking $\sim$250 min to reach the chamber. At 0 min, the surfactants first reach the chamber. Note that these times should not be confused with t_0 in Fig. 1, which represents the time of confluency on the droplets. (B) The normalized perimeter (P^*), measured at the drop equator, is plotted versus time. (left) Evolution of $P^* = P/P_0$ for drops not exposed to surfactants; here, P_0 is the initial perimeter (solid line and filled area: mean $\pm$ SD; n=15 drops). To synchronize the time axis with the influx of surfactants in this experiment, we plot the control group from ~ -250 min. (right) Evolution of $P^* = P/P_f$ for the test group, where P_f is the final perimeter. At $\sim$280 min, biofilms abruptly detach and the drops become spherical. The thick magenta line represents the mean value, while the lines represent different droplets (n = 8 drops). As in (A), the surfactants first reach the chamber at 0 min. Fluctuations in individual P^* curves arise due to rotation of the droplets in traps. The cyan shading indicates surfactant concentration at the outlet of the drop chamber (see fig. S2A for location), and reaches 95% of the steady-state concentration at $\sim$120 min, which we determine by calibrating the device. To generate DBs, we culture the test group for $\sim$240 min prior to 0 min. (C) The air/water surface tension (γ_{AW}) as a function of concentration of our mock Corexit dispersant mixture (solid line and filled area: mean $\pm$ SD; n=3). See Methods for composition. We estimate CMC = 0.001 wt% and the arrow indicates 50xCMC. (D) Oil-water interfacial tension between ONR7a media and C16 containing different concentrations of mock Corexit (mean $\pm$ SD; n$\geq$3). The bar labeled ONR7a is the control test. We normalize concentrations by the CMC, which was determined in (C). (E) Calibration curve for our device used to estimate the concentration of the dispersants as a function of time. Fluorescence intensity is recorded as function of time at the chamber outlet using 3 μM FITC dissolved in the media containing mock Corexit (1xCMC) infused at 0.5 μL/min. The solutes take $\sim$240 min to travel from the syringe to the chamber, requiring another $\sim$115 min to reach 95% of the steady state concentration (dashed line). In this test, we designate 0 min as the point when fluorescence is detectable at the chamber outlet. Methods are described in Sec. 3.7

.

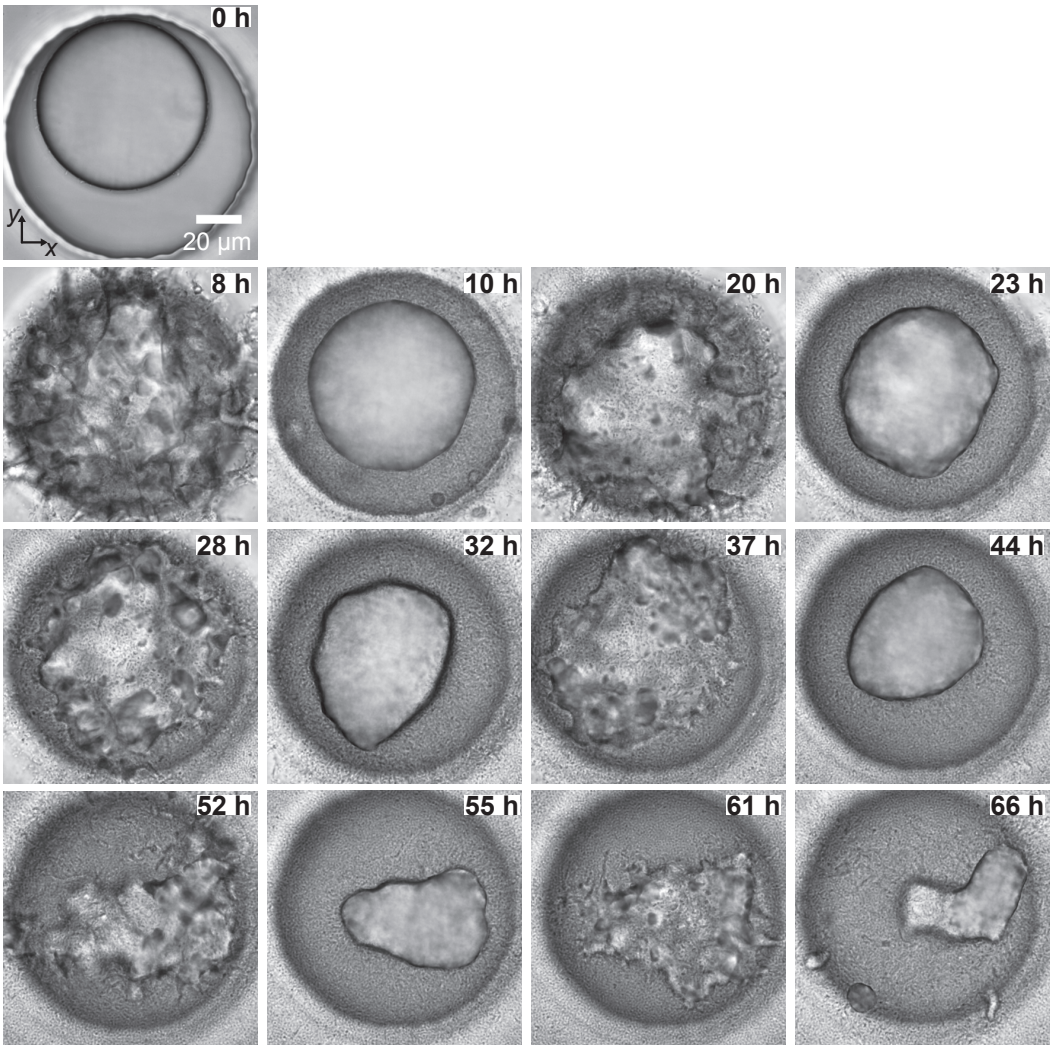

Fig. S9: Bright-field image sequence showing biofilm oscillations. Oscillatory phase on a representative droplet (see movie S5). A cell monolayer is formed at 0 h. Over the course of the next 65 h, the biofilm phenotype oscillates between the SB and DB phases. The time-points at 10 h, 23 h, 32 h, 44 h, 55 h, 66 h (resp. 8 h, 20 h, 28 h, 37 h, 52 h, 61 h) are chosen as local minima (resp. maxima) of the oil/water interface length.

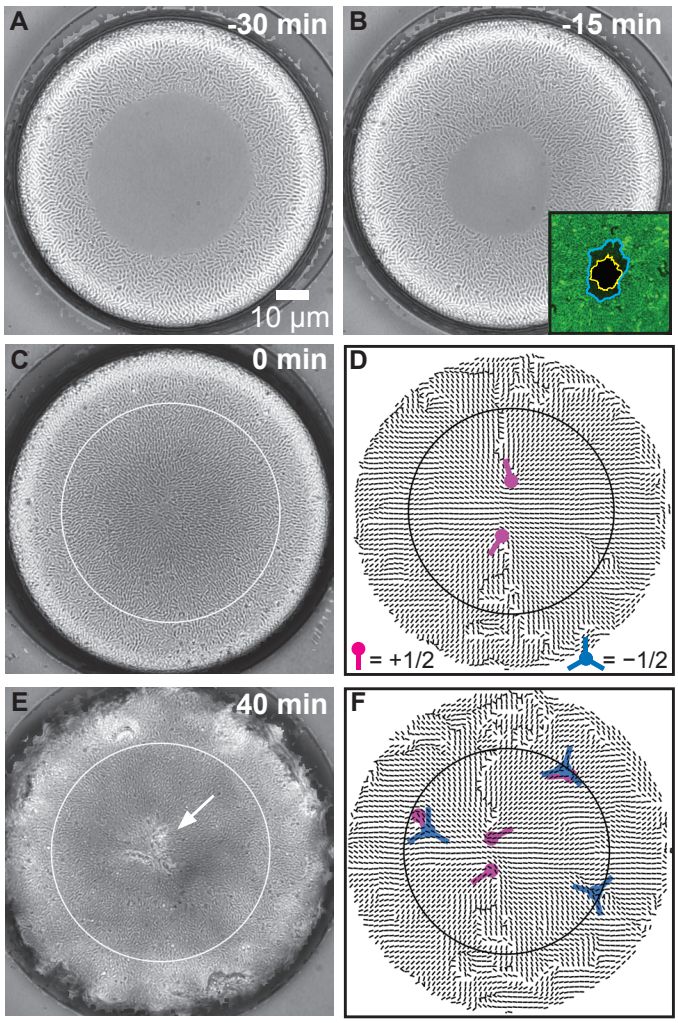

Fig. S10: Defect-mediated dimple formation in flattened drops. Flattened droplets develop two closely spaced +1/2 topological defects at t_0. All brightfield images are extended focus images taken at the bottom of the flattened droplet shown in Fig. 4. Acquisition times are indicated. (A,B) Interfacial tension of the droplet excludes cells from a circular region at the bottom of the droplet. (B, inset) Confocal image showing the excluded region at the bottom of the droplet, outlined in blue. Through this hole, the excluded region at the top of the drop, outlined in yellow, is visible. (C) Pressure in the cell layer due to division drives cells into the excluded region, generating a monolayer. The circle indicates the flat region of the droplet due to contact with the underlying cover glass. (D) The director field for the image in (C) and two closely spaced +1/2 defects (magenta comet icon) are shown. (E) A dimple forms at the center of the flat region, indicated by the arrow. (F) The director field for the image in (E) with +1/2 defects (magenta comet icon) and -1/2 defects (blue trefoil icon).

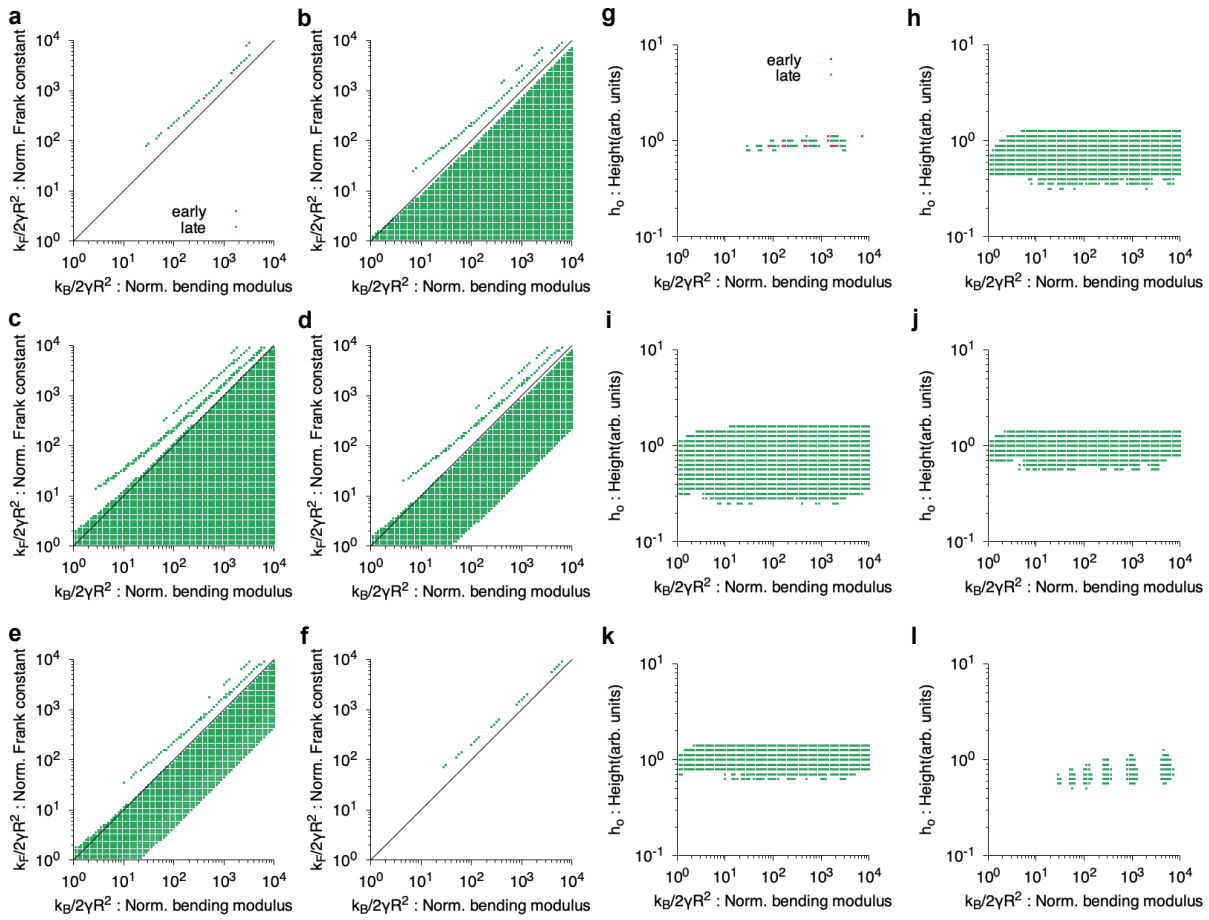

Fig. S11: Error function dependence on parameter space. Region of the parameter space whereby the error function $\mathcal{E}$ (Eq. (79)) is at most 20% larger than the absolute minimum error $\mathcal{E}_{\min}$. Panels (a-f) show a cross-section of the parameter space on the plane $\kappa_B/2\gamma R^2$-$\kappa_F/2\gamma R^2$, and panels (g-l) on $\kappa_B/2\gamma R^2$-h_0. The experimental cases are ordered from a-f and g-l as in table S2.

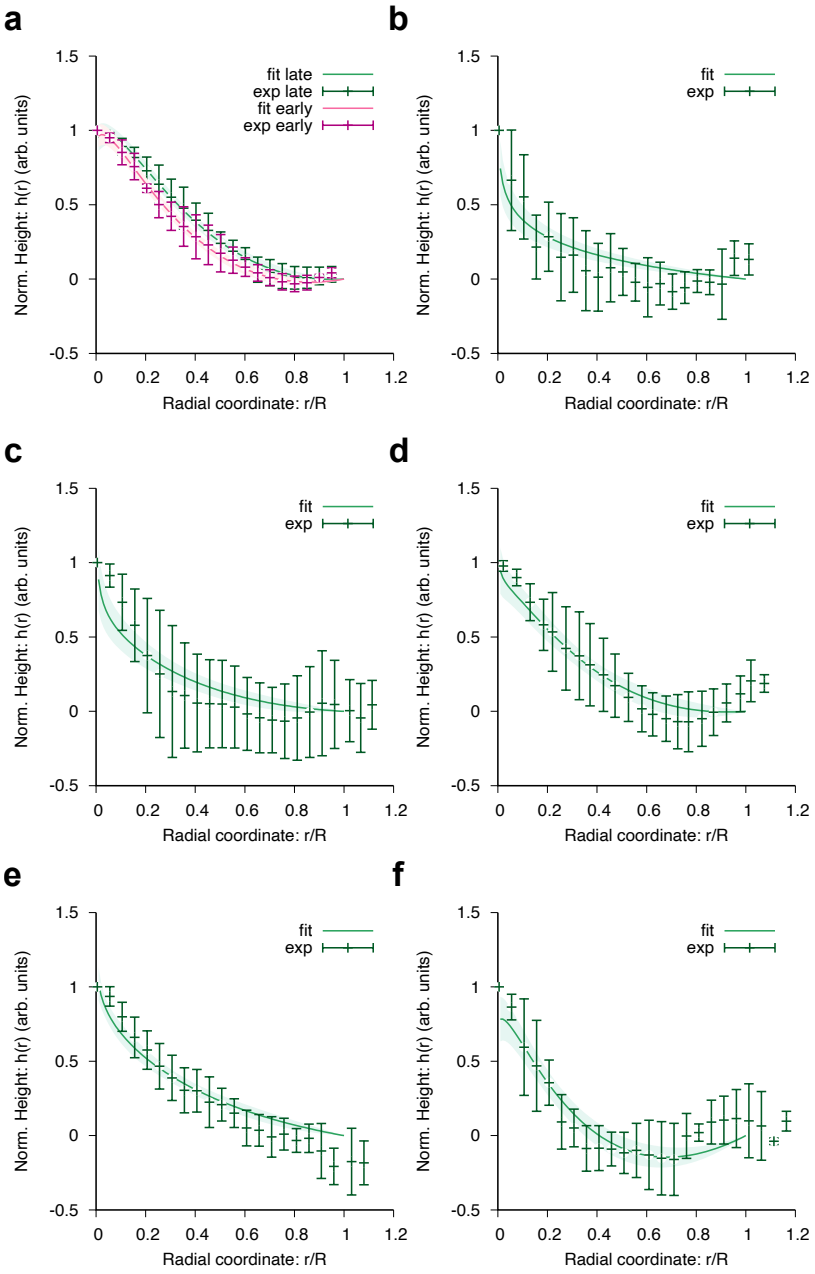

Fig. S12: Theoretical fits to experimental data. (a-f) Dimple profiles as a function of the radial coordinate r/R. In (a-f), the green lines are theoretical fits while the dark green points are experimental profiles ($\mathrm{n} = 4$). In (a), the magenta line is a theoretical fit while the dark magenta points are experimental profiles ($\mathrm{n} = 4$). Error bars in theoretical fits, which are represented as shaded areas, correspond to the standard deviation of parameter values that lead to $\mathcal{E} < 1.2\mathcal{E}_{\mathrm{min}}$ and are then averaged in time. In the experimental curves, the error bars correspond to the standard deviation for $\mathrm{n} = 4$ that are averaged in time. In experiments, the averaged dimple radius ranges from $R = 25 - 35$ μm, while the averaged height ranges from $h = 4 - 8$ μm.

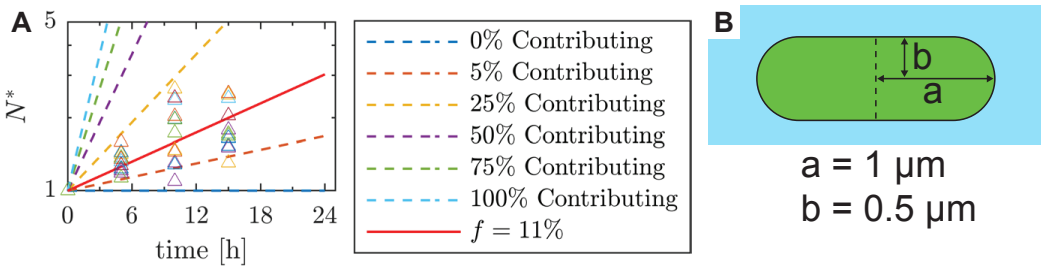

Fig. S13: Estimated number of interfacial cells driving the increase in surface area. (A) We plot the normalized number of interfacial cells (N^*) for DBs as a function of time. N^* is calculated from the surface area data of the 10 oil droplets shown in Fig. 1D using Eq. (8). The initial value of N^* (=1) represents the number of cells in the confluent layer at buckling. The (Δ) represent the calculated values, the solid line is the best fit to the data by fitting the predicted number of cells that reside at the droplet surface assuming that only a percentage of cells of all cells participate in expanding the interface (from Eq. (7)), and the dashed lines show the predicted number of cells that would reside at the interface, assuming that only a percentage (f) of all cells participate to expand the interface. These cells may be lost from the interface during each division cycle and thus are not active participants in the interface. (B) Typical dimensions of an *A. borkumensis* cell when cultured using C16 as the carbon source.

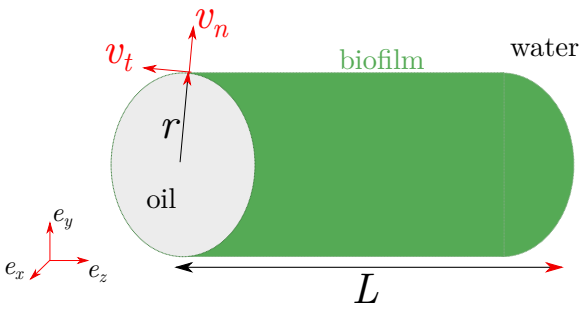

Fig. S14: Geometry of a model biofilm-stabilized tube. The tube has a constant radius r, the base-to-tip length is given by L, and it ends with a half-spherical cap of radius r.

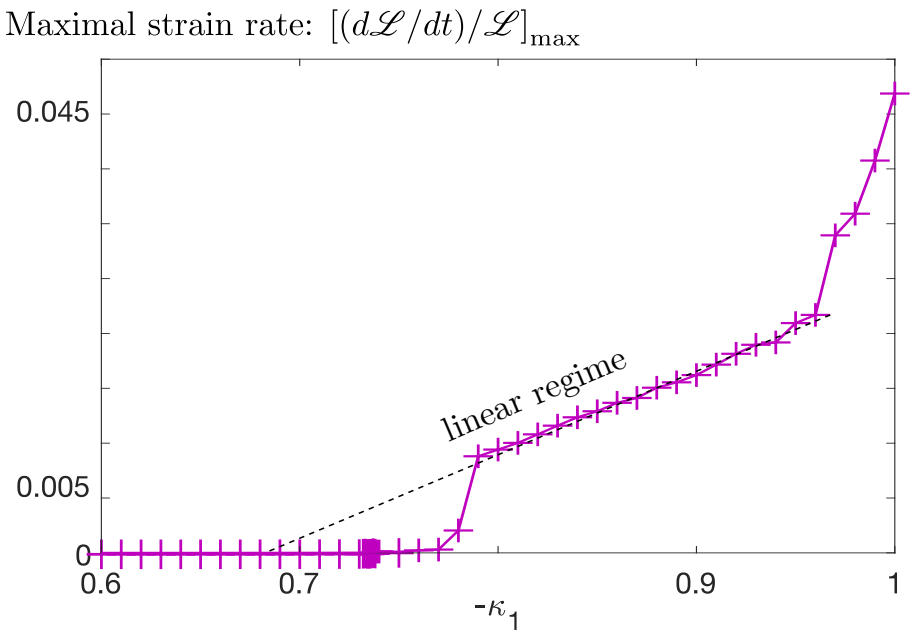

Fig. S15: Phase-field model with no coupling to the bacteria density. The maximal strain-rate, defined as $\dot{\mathscr{L}}/\mathscr{L}$, where $\mathscr{L}$ is the interface length (Eq. 65) is plotted as a function of a fixed effective surface tension parameter κ_1 (linear scale).

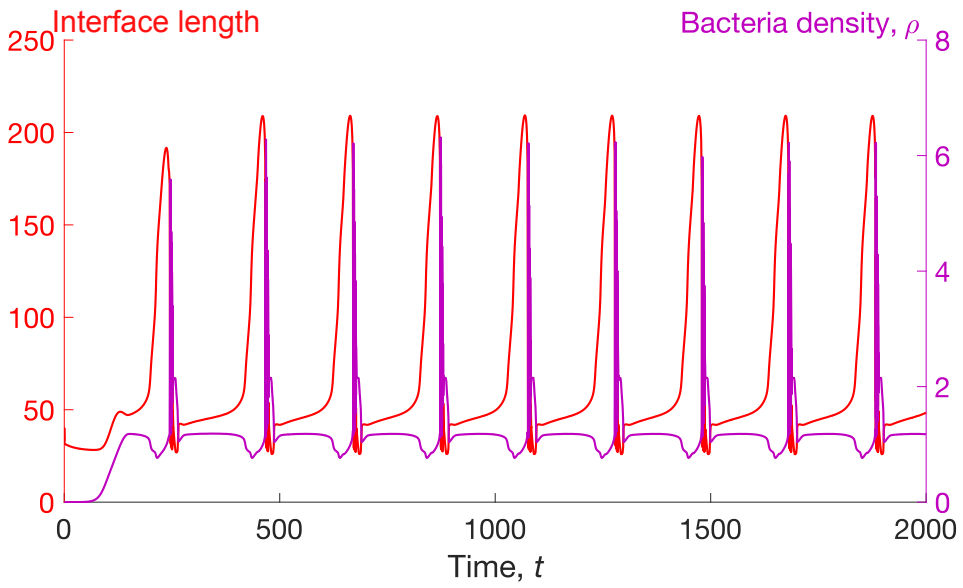

Fig. S16: Phase-field model with coupling to the bacteria density. Time evolution of the total interface length $\mathscr{L}$ (red, left axis) and density ρ (magenta, right axis) for the oscillatory regime parameter set, $k_1 = 5.4, \rho_H = 1.2$, with all other parameters fixed in Sec. 7.5 (movie S4). During the rapid tube expansion phase, the density is lower than $\rho_H = 1.2$.

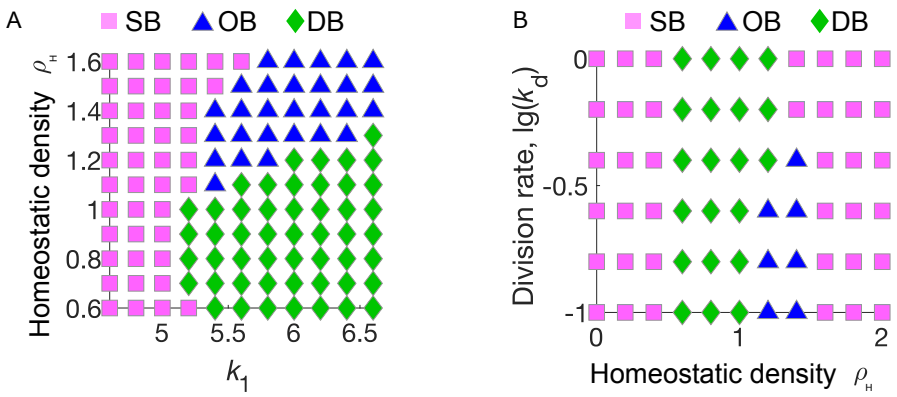

Fig. S17: Phase-field model with coupling to the bacteria density. (A-B) Phase diagrams of the modeled spherical biofilm (magenta squares), oscillatory biofilm (blue triangles) and dendritic biofilm (green diamonds) phenotypes as a function of model parameters (A) ρ_H and k_1 and (B) k_1 and ρ_H.

Table S1: Interfacial tensions of the different phases measured in this study. The control tests (fresh C16 versus fresh ONR7a) has an γ = 30.9 $\pm$ 1.4 mN/m.

	Interfacial Tension γ (mN/m) of respective fractions		
	Cond. oil vs Fresh media	Cond. media vs. Fresh oil	Cells (Fresh media) vs. Fresh oil
SB Phenotype	20.6 $\pm$ 2.1	19.8 $\pm$ 0.8	19.6 $\pm$ 1.4
DB Phenotype	7.4 $\pm$ 1.6	24.7 $\pm$ 2.0	24.3 $\pm$ 3.9

Table S2: Estimation of material parameters for a membrane with nematic order. The dimensionless parameter κ_F/κ_B corresponds to the ratio between the energetic cost due to distortion of the director field and due to bending deformations. The error bars correspond to the standard deviation in the region of the parameter space that satisfies $\mathcal{E} < 1.2 \times \mathcal{E}_{\min}$. In the first experiment (number 1), the 'early' condition corresponds to height profiles at $t = 20$ min post-confluency, whereas the 'late' condition is at $t = 26 \pm 3$ min post-confluency. In fig. S12, 'Early' and 'Late' are the green and magenta curves, respectively.

Parameter	#1 Early	#1 Late	#2	#3	#4	#5	#6
κ_F/κ_B	1.8 ± 0.2	2.0 ± 0.4	< 4	< 5.5	< 5	< 4	1.7 ± 0.3
h_0(arb. units)	1.0 ± 0.1	0.9 ± 0.1	0.8 ± 0.2	1.0 ± 0.3	1.1 ± 0.2	1.1 ± 0.2	0.8 ± 0.2

Table S3: Nucleotides used in this study.

Name	Sequence (5' to 3')	Notes
abo-gap -526 Fw	CCTTggatccCCCCACCAGTTCATCAAAGG	Amplification of P_{gap}
abo-gap +39 Rv	CTCTgaattcACCGTTGATGGCAATGCGAA	Amplification of P_{gap}
pPROBE-GT inv Rv	catatgtttttcctccttataaagttaatctttag	Amplification of pPROBE-GT
pPROBE-GT inv Fw	ctatacaaataggaattaattccaggca	Amplification of pPROBE-GT
mCherry IF Fw	actttataaggaggaaaaacatatgAGCAAGGGCGAGGAGAACAA	Amplification of mCherry
mCherry IF Rv	ctggaattaattcctatttgtatagCTCGTCCATACCCCCAGTCG	Amplification of mCherry

Table S3: Nucleotides used in this study.

Name	Sequence (5' to 3')	Notes
mCherry-2L-Pa	ATGAGCAAGGGCGAGGAGAACAA CCTGGCGATCATCAAGGAGTTCAT GCGCTTCAAGGTCCACATGGAAGG CTCCGTCAATGGCCACGAGTTCGA GATCGAAGGCGAGGGCGAAGGCC GTCCGTACGAAGGCACCCAGACG GCCAAGCTGAAGGTCACCAAAGGC GGACCGCTTCCGTTCGCCTGGGA CATTCTGAGCCCGCAGTTCATGTA CGGGTCGAAGGCCTACGTGAAGC ATCCGGCCGACATCCCGGACTACC TGAAGCTGAGCTTCCCGGAAGGG TTCAACTGGGAACGGGTGATGAAC TTCGAGGATGGCGGCGTTGTCACC GTAACCCAGGACAGCTCGCTCCAA GACGGCGAGTTCATCTACAAGGTG AAGCTGCGCGGCACCAACTTCCCC AGCGATGGTCCGGTCATGCAGTGC CGCACGATGGGCTGGGAGGCCAG TACCGAGCGCATGTATCCCGAAGA TGGCGCGCTGAAGGGCGAGATCA AGCAGCGGCTCAAGCTCAAAGACG GTGGCCACTATGACGCGGAAGTGA AGACCACCTACAAGGCCAAAAAGC CCGTGCAGTTGCCAGGCGCGTAC AACGTGGACATCAAGCTGGACATC CTGTCCCACAACGAGGACTACACC ATCGTCGAGCAGTACGAGCGCGC AGAAGGCCGCCATTCGACTGGGG GTATGGACGAGCTGTACAAGTGA	mCherry ORF

Movie S1: Spherical biofilm (SB) phenotype. Bright-field time-lapse sequence over 87 hours (3.6 days) of a chamber with a trapped oil droplet, corresponding to fig. S3B. Cells harvested from 1 day culture in ONR7a+C16 developed SBs. The cells develop a confluent layer on C16 droplets at the time t = 0.

Movie S2: Dendritic biofilm (DB) phenotype. Bright-field time-lapse sequence corresponding to fig. S3C. Cells harvested from some of the 5-day cultures in ONR7a+C16 developed DBs.

Movie S3: Effect of 50xCMC concentration of a surfactant mixture similar in composition to Corexit 9500 dissolved in the growth medium on a dendritic biofilm (DB) aged 4 h post confluency. The surfactant enters in the device at t = 0, full time-lapse sequence corresponding to fig. S8.

Movie S4: Oscillatory biofilm (OB) phenotype. Full time-lapse sequence corresponding to Fig. 3G in the main text and to fig. S9.

Movie S5: Phase-field simulations in the (left) spherical biofilm (SB) regime, $k_1 = 5.0, \rho_H = 1.2$; (middle) oscillatory biofilm (OB) regime, $k_1 = 5.4, \rho_H = 1.2$; (right) stable dendritic biofilm (DB) regime, $k_1 = 5.4$, $\rho_H = 1.0$, with all other parameters fixed in Sec. 7.5.

Movie S6: Bacterial invasion of the flat regions at the bottom of a squeezed droplet followed by biofilm-mediated droplet dimpling. Time-lapse sequence of a droplet undergoing buckling similar to that shown in Fig. 4 and fig. S10.